OPTICAL STUDIES OF ZnO GROWN BY METALORGANIC CHEMICAL VAPOUR DEPOSITION

by

Zhiwei Deng

B.Sc., University of Science and Technology of China, 2008

THESIS SUBMITTED IN PARTIAL FULFILLMENT

OF THE REQUIREMENTS FOR THE DEGREE OF

MASTER OF SCIENCE

IN THE DEPARTMENT

OF

PHYSICS

SIMON FRASER UNIVERSITY

Spring 2012

APPROVAL

Name: Zhiwei Deng

Degree: MASTER OF SCIENCE

Title of Thesis: OPTICAL STUDIES OF ZnO GROWN BY METALORGANIC CHEMICAL VAPOUR DEPOSITION

Examining Committee:

Dr. Jeffrey McGuirk
Assistant Professor, Department of Physics, SFU
(Chair)

Dr. Simon P. Watkins, Senior Supervisor
Professor, Department of Physics, SFU

Dr. Mike Thewalt, Supervisor
Professor, Department of Physics, SFU

Dr. Patricia M. Mooney, Supervisor
Professor, Department of Physics, SFU

Dr. Gary Leach, Internal Examiner
Associate Professor
Department of Chemistry, SFU

Date Approved: February 2,2012

Partial Copyright Licence

Abstract

The controlled n-type and p-type doping of ZnO is an ongoing and challenging field of study which needs to be resolved before this material can fulfill its great promise as an optoelectronic material. Metalorganic chemical vapour deposition (MOCVD) is a process that has been extensively investigated for ZnO growth. However, there have been very few reports of high resolution photoluminescence (PL) spectroscopy for MOCVD grown ZnO. In this thesis, strong donor bound exciton transitions with linewidths as low as 0.2 meV were observed in a 4.2 K low temperature PL spectrum of nominally undoped ZnO epilayers grown with dimethylzinc (DMZn) and nitrous oxide (N_2O) at 800 °C on *c*-plane sapphire substrates by MOCVD. Intentional n-type doping of ZnO by MOCVD with group III dopants such as In and Al at high growth temperature has been studied. The addition of controlled amounts of In and Al precursors allows us to unambiguously observe donor bound exciton emission from these impurities which results in identification of the dominant residual donor in nominally undoped ZnO to be Ga and to infer the residual compressive strain in the layers due to lattice mismatch between ZnO and the sapphire substrate. PL measurements on ZnO epilayers annealed in oxygen at $900-1000$ °C show that group III dopants are quite mobile at temperatures above 800 °C. Raman scattering spectroscopy measurements were performed to investigate the vibrational properties of MOCVD grown ZnO. Strong and broad vibrational modes due to sp^2 graphitic carbon clusters were found in the Raman spectrum of low growth temperature ZnO epilayers at around 1350 cm^{-1} and 1600 cm^{-1}. At high growth temperatures (>700 °C), the graphitic modes disappear and the spectrum is dominated by ZnO lattice phonons.

Dedication

to my family and my girlfriend

Acknowledgments

I would like to thank my senior supervisor, Prof. Simon Watkins, for his guidance and support on this research. His patience and encouragement are the main factors that make this work and the completion of this thesis possible.

I am grateful to the members of my supervisory committee, Prof. Mike Thewalt and Prof. Patricia Mooney, for their guidance and feedback during this project. I am thankful to Dr. David Huang who grew and prepared the ZnO samples investigated in this work. Dr. Michael Chen deserves my gratitude, as he instructed me to use the micro-Raman spectrograph in his lab and provided great help whenver I met a problem during the Raman measurements. I would like to thank Riley Schick-Martin for help on setting up the photoluminescence spectrograph. I would like to give my acknowledgements to my group members, David Lackner, Dichen Li, Ian Anderson and Omid Salehzadeh Einabad, for their help and patient discussion during this research.

I would like to thank my friends and brothers, Chao Liu, Dichen Li, Jixin Liang, Wen Huang, Yiwei Zhang and Zenan Jiang. Without their friendship and support, it would be hard for me to face and enjoy life in a foreign country. The joyful hiking and ice skating, lovely evenings and wonderful tours will be the most beautiful memory in my life.

Contents

List of Tables

List of Figures

Chapter 1

Introduction

The semiconductor zinc oxide (ZnO) is an ongoing and challenging field of study in the research community for recent decades due to a number of advantages it offers. Firstly, ZnO has a relatively large direct band gap of 3.37 eV at room temperature. Similar to GaN, another wide band gap semicondutor ($E_g = 3.4$ eV at room temperature), ZnO can potentially be used for fabricating semiconductor light emitting devices with wavelengths in the green, blue, and ultraviolet regions [1]. Secondly, the free exciton binding energy in ZnO is as high as 60 meV [2], which is 2.4 times that of the room temperature thermal energy ($k_BT = 25$ meV). This special characteristic of ZnO promises an efficient and intense near-band-edge excitonic emission even under low excitation intensity at room or higher temperatures. A number of reports on laser emission from ZnO-based structures at room temperature and beyond have been published [3, 4, 5, 6]. Thirdly, fairly high-quality single crystal substrates are available for large scale homoepitaxial ZnO thin film growth [7]. Besides the above mentioned properties, there are other advantages that make ZnO potentially superior to other wide band gap materials. As several kinds of crystal growth technologies are widely investigated for ZnO [8, 9, 10], there exists the potential to manufacture large-quantity low-cost ZnO-based devices. The stability to high energy radiation has been reported by several groups for ZnO [11], which provides an opportunity for space applications. Due to the fact that ZnO can be easily etched with wet chemical etchants [12], it is a suitable material for fabrication of small-size devices. In addition, ZnO can be used as a substrate for high-quality GaN epilayer growth [13] for the reason that these two materials have the same crystal structure and very similar lattice parameters.

ZnO is a II-VI compound semiconductor, with ionicity intermediate between a covalent semiconductor and an ionic semiconductor. ZnO can be formed in three different kinds of crystalline structures: wurtzite, zinc blende and rocksalt, but the wurtzite structure is the most stable thermodynamically. The unit cell of ZnO with the wurtzite structure is depicted in Fig. 1.1. This unit cell is hexagonal with two lattice parameters, a = 3.24986Å and c = 5.20659Å [14], and belongs to the space group of $P6_3mc$. In our work, epitaxial ZnO thin films were grown on *c*-plane sapphire substrates by metal organic chemical vapor deposition (MOCVD).

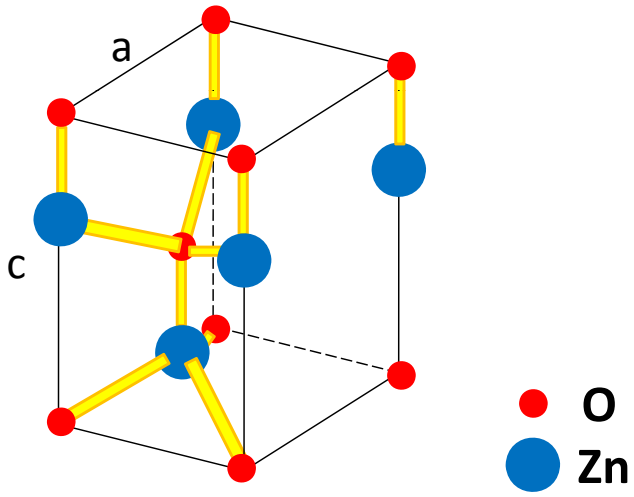

Figure 1.1: Unit cell of ZnO crystal with the hexagonal wurtzite structure.

In order to attain the potential offered by ZnO material, both high-quality n-type and p-type ZnO will be required for the development of p-n homojunctions. Nominally un-

doped ZnO shows intrinsic n-type conductivity with a high electron concentration of about 10^{18} cm^{-3} [15]. However, it is still uncertain whether native defects such as zinc interstitials (Zn_i) and oxygen vacancies (V_O) or hydrogen impurities are responsible for the high n-type conductivity. Impurities in II-VI semiconductors play an important role in the electrical properties. Impurity atoms can be introduced into the host material by a process called doping. Two kinds of lattice sites can be occupied by the dopant atoms: one, the site of the host atoms (substitutional impurities); the other, the site between the host atoms (interstitial impurities). Depending on the valence electrons of the dopant and the occupied lattice site, the dopant impurites can work as donors or acceptors giving rise to n-type or p-type conductivity, respectively. Reproducible, reliable and high-conductivity p-type ZnO material is difficult to achieve and has been the main obstacle on the way to the application of ZnO [16]. This difficulty is due to a number of reasons. First, the dopants are likely to be compensated or passivated by the native defects or background impurities [17]. The low solubility of the dopants in ZnO can be another possible cause [18]. Also, for the case of common intentional n-type doping, the physical location of the doping elements and the role they play in the n-type conductivity of ZnO material is still not clear [19, 20, 21]. The exact role of intrinsic and extrinsic defects and impurities in ZnO material is yet to be determined.

The work in this thesis is focussed on the structural, optical and vibrational properties of epitaxial ZnO thin films grown by MOCVD on *c*-plane sapphire substrates. Chapter 2 gives a brief introduction to the experimental techniques which were used to grow and measure the ZnO epilayers, including metalorganic chemical vapour deposition (MOCVD), Raman scattering spectroscopy, and photoluminescence (PL) spectroscopy. Chapter 3 presents PL experimental data. A brief introduction to the physics of the PL transitions is presented first. Then 4.2 K low temperature PL data for nominally undoped and intentionally In-doped ZnO are discussed to identify the impurity atoms in the ZnO material and to infer the residual compressive strain in the layers. The temperature dependent PL data for In-doped ZnO are also discussed here. In the following part, low temperature PL data are discussed to study the effect of aluminum doping, growth temperature, and annealing on the optical and structural properties of ZnO epilayers. Chapter 4 introduces another useful technique-Raman spectroscopy. The theory of Raman scattering, selection rules, and local vibrational modes is briefly introduced first. Then Raman scattering data are discussed

to study the effect of growth temperature, annealing, and carbon doping on the electronic and vibrational properties of ZnO. In the final chapter, all the experimental results are summarized and possible future directions of this research are given.

Chapter 2

Experimental Methods

In this chapter a brief introduction to the experimental methods used for the growth of ZnO epilayers is outlined. The technique used to grow epitaxial ZnO thin films in this work is metalorganic chemical vapour deposition (MOCVD) (which is also known as organometallic vapour phase epitaxy (OMVPE)). In addition, two different kinds of spectroscopic techniques were used to obtain the experimental data in this thesis. The first is Raman scattering spectroscopy. Raman scattering is a form of inelastic light scattering by phonons or other collective excitations, usually achieved with a high intensity light source such as a laser. The scattered beams consist of two parts: one, called Rayleigh scattering which has the same frequency as the incident beam is dominant; the other, called Raman scattering has a frequency shift and is weak compared with the incident beam. In Raman spectroscopy, the frequency shifted light is what we are interested in. The second technique is photoluminescence (PL) spectroscopy. In PL spectroscopy, the sample is excited by absorption of light with photon energy greater than or equal to the band gap of the material. The luminescence light is then detected as a function of wavelength. The PL process consists of three steps: first the material absorbs photons of the incident light and produces electron-hole pairs; then the excited electron-hole pairs thermalize down to the extrema of the band gap and form bound states called excitons; finally the excitons recombine and emit photons which have lower energies compared with the incident photon.

2.1 Metalorganic chemical vapour deposition

MOCVD is a widely used method to grow epitaxial layers or structures on a single crystal substrate. The precursors are usually organometallic chemicals which consist of a source atom surrounded by organic radicals. The organometallic precursors are usually in the liquid state and stored in stainless steel containers (called bubblers). The precursor molecules need to be transported by a pure carrier gas such as nitrogen used in this work. The vessel used to store the precursor has an inlet tube that reaches down into the organometallic liquid and an outlet tube that stays above the organometallic liquid. The carrier gas flows through the inlet tube, collects the reactant molecules and then leaves from the outlet tube. After that the carrier gas which is saturated with the vapour of the precursor flows into the reaction chamber. The amount of the precursor extracted can be adjusted by the control of the bubbler temperature, bubbler pressure and flow rate of the carrier gas.

In the growth chamber, a stagnant boundary layer of carrier gas resides directly adjacent to the heated substrate, which is placed on a susceptor that in our case is heated by a resistance heater. The temperature is monitored by a thermocouple inserted into the susceptor. The reactant molecules diffuse through the boundary layer to the surface of the substrate. When the molecules approach the surface, they are heated and undergo pyrolysis - decomposing into source elements and organic radicals. After or during the pyrolysis, the source radicals are physisorbed to the surface by weak Van der Waals forces and then migrate to find a site where they can form multiple chemical bonds and be incorporated into the crystal.

The Zn precursors used for the growth of epitaxial ZnO thin films in this thesis were dimethylzinc (DMZn, $(CH_3)_2Zn$) or diethylzinc (DEZn, $(C_2H_5)_2Zn$). For intentional n-type doping, trimethylindium (TMIn, $In(CH_3)_3$) was used as the In precursor and alane trimethylamine (TMAA, $AlH_3N(CH_3)_3$) was used as the Al precursor. The carrier gas used in this work is pure nitrogen. The substrates used for the deposition were c-plane sapphire and (111) silicon single crystals. In this machine, a standard reactor pressure of 700 Torr was always chosen during the growth.

2.2 Raman scattering spectroscopy

Raman scattering measurements were taken in Dr. Chen′s laboratory at Simon Fraser University. The spectrometer is a Horiba Jobin Yvon LabRAM 300 instrument. It is an integrated Raman system. The microscope is coupled confocally with the spectrograph, which means the focal points of the sample and the entrance slit of the spectrograph share the same location. A schematic view of this spectrometer is shown in Fig. 2.1.

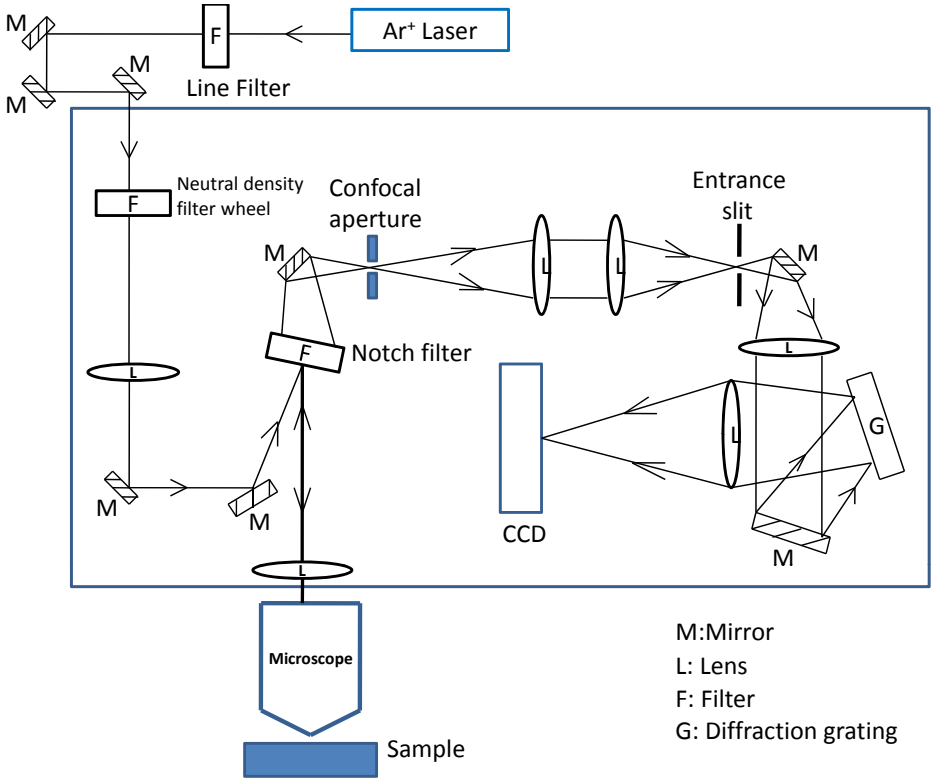

Figure 2.1: A block diagram of the LabRAM 300 Raman spectrometer. Ray optics are only shown in detail from the notch filter on.

2.2.1 Instrument

Two kinds of lasers were used as the light source in our Raman measurements. One is the He-Ne laser, with a wavelength of 632.817 nm and a fixed power of 20 mW. The other is an Ar ion laser with several available laser lines. We used the 457.800 nm and 514.532 nm lines and the power was adjustable with a maximum value of 1.5 W. The microscope is an Olympus BX40 research microscope with a minimum spot size of 1 μm. We used a 100$\times$ objective with a numerical aperture of 0.9. A notch filter was used to cut off light with a wavenumber shift below 120 cm^{-1} in order to reject the laser line. This instrument uses the Stigmatic 300 mm focal length spectrograph. Two kinds of gratings were available, one was 1800 grooves/mm and the other was 600 grooves/mm. This allows us to choose different measurement resolutions. The grating disperses the light onto a Peltier thermo-electric cooled charge coupled device (CCD) with a pixel size of 27 μm and an array size of 1024×256 pixels.

2.2.2 Methods

All the Raman scattering measurements in this work were taken at room temperature. Before each run, a silicon reference sample was used to calibrate the spectrometer by means of the Si longitudinal optical (LO) phonon peak located at 520.07 cm^{-1}. When the Ar ion laser was used as the light source, the laser power was set to be 100 mW. Because of multiple reflections and refractions due to the many optical elements, the power of the laser line was reduced to about 10 mW when it reached the sample. Although the incident laser beam was polarized, there was no polarization filter mounted before the spectrograph entrance slit in our LabRAM 300 system. Therefore, we didn$'$t select the polarization direction of the scattered line before it was detected by the CCD for our Raman scattering measurements.

The Rayleigh radiation scattered from the sample was blocked by the notch filter. The Raman scattered radiation was focused onto the confocal aperture. Through the lens array, the scattered light was then imaged onto the spectrometer entrance slit. The aperture of the beam was adapted by the lens array to match with that of the spectrometer, so that the scattered beam could exactly cover the whole grating plate. The grating separated the scattered light into wavelength components which were transmitted to different pixels of the CCD detector. The resolving power of the spectrometer was highly dependent on the

chosen grating. For a grating with a ruling spacing of 1800 grooves/mm, the resolution of the spectrometer was 1.6 cm^{-1}; With a smaller ruling spacing of 600 grooves/mm, the resolution was decreased to 4.8 cm^{-1}.

2.3 Photoluminescence spectroscopy

A schematic view of the PL system used in this thesis is shown in Fig. 2.2. This PL system consists of the light source, the optics, the cryostat, the spectrograph, the detector and the control electronics. All the PL measurements in this thesis were taken in a dark environment. This PL system could distinguish and collect signals ranging from ultraviolet (UV) light to the visible light region.

2.3.1 Light source and optics

The light source used in our PL system is the 325.031 nm line of a He-Cd laser with a total power of 25 mW. The photon energy of this laser line is 3.814 eV which is higher than the bandgap of ZnO with a value of 3.437 eV at 4.2 K. Two filters are used to cut off the other laser lines and visible light so that highly narrow spectrum laser light is produced. A fused silica lens $NT48-314$ with a focal length of 500 mm is available to focus the laser spot before it reaches the sample if necessary. The reflecting mirrors are UV laser mirrors $NT48-016$ with a diameter of 25.4 mm. The mirror used to collect the luminescence light from the sample is a UV enhanced aluminum $1/4$ wave mirror $NT45-340$ with a size of 75 mm $\times$ 75 mm. The collecting luminescence is then focussed by a quartz lens with a diameter of 50 mm, and its focal length is 150 mm.

2.3.2 Cryostat

The sample is mounted on a copper block in a Janis Varitemp dewar, in which the sample is cooled by gas flow from a liquid helium reservoir. The temperature can be regulated between 4.2 K and room temperature by a LakeShore temperature controller. A silicon diode sensor is used to monitor the temperature of the sample, and this information is fed back to the temperature controller to regulate the power of a resistive heater. For this kind

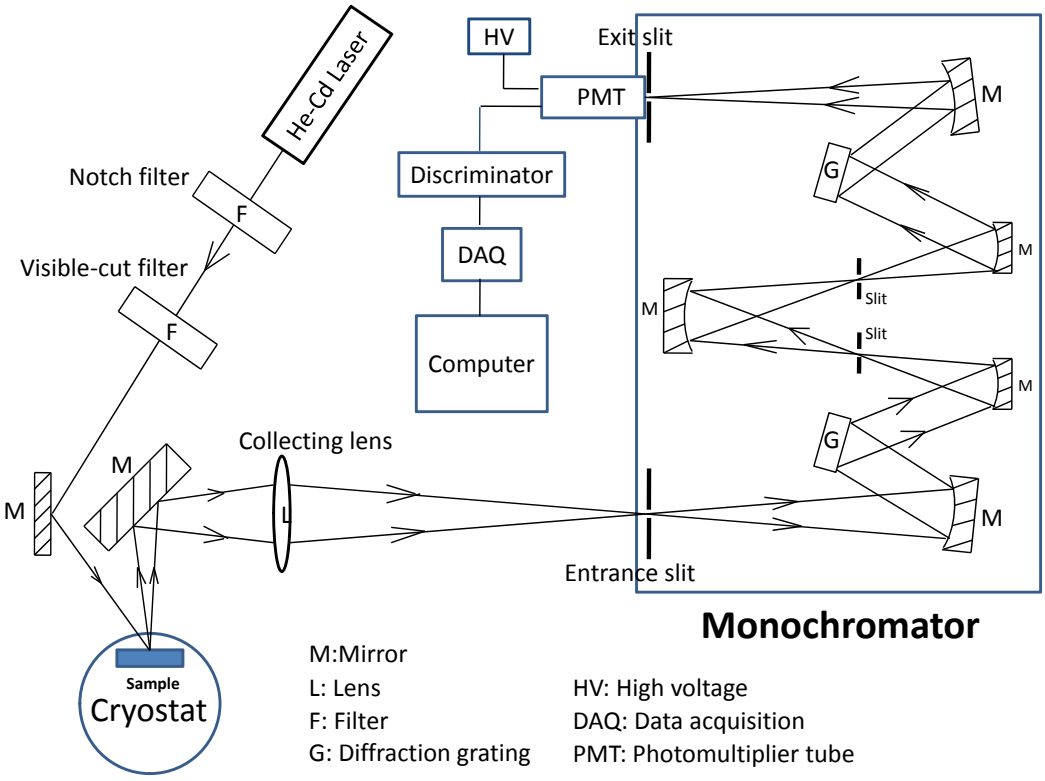

Figure 2.2: A block diagram of the photoluminescence spectroscopy system.

of temperature sensor, the working range is from 1.4 K to 325 K. With this temperature controller, we can maintain the nominal sample temperature within less than 0.01 K of the set point. In addition, we can cool the sample to as low as 2.17 K by pumping the liquid He in the sample chamber with the control valve closed.

2.3.3 Spectrograph and detector

The luminescence is analyzed by a SPEX 1404 double monochromator with a 0.85 m focal length. The two gratings have a ruling spacing of 1200 grooves/mm and are mounted in the Czerny-Turner configuration. The grating angles are controlled by a stepper motor system. The entrance and exit slits of the spectrometer are used to control the resolution of the measurements, so the widths are chosen according to the requirement of the specific run. The height of the entrance slit can also be selected, but for all of our measurements we fixed it at 0.2 cm. The two center slits shown in Fig. 2.2 are set to block the stray light from entering the second half of the monochromator, which improves the rejection of the laser line when using the system for Raman measurements. For all of our measurements, the central slits are set to 1 mm. The detector used to analyze the luminescence in this study is a Hamamatsu R585 photomultiplier tube (PMT) with a spectral response ranging from 160 nm to 650 nm. Its maximum response wavelength is 420 nm. This tube has a 5 mm $\times$ 8 mm bialkali photocathode with a sensitivity of 50 mA/W at 420 nm for photon counting.

2.3.4 Control electronics

The gratings are moved by the stepper motor interface (Mini-step driver, MSD) which receives digital pulses from a National Instruments-NI USB 6211 data acquisition module. This NI USB device controls the movement of the MSD by a series of electric pulses which tell the gratings how far to move, and a voltage signal which determines the direction of motion for the gratings. Another voltage signal is transmitted to control the status of a shutter which is adjacent to the exit slit in the monochromator. This signal keeps the shutter closed until the gratings move to the position where the PMT starts to receive the requested luminescence light. This action helps to protect the PMT as it prevents the laser line from irradiating the photocathode. In addition, the NI USB device is also in charge of

accumulating and recording the counts of the emitted photons detected by the PMT as a function of wavelength. A high voltage is supplied to the PMT to accelerate and amplify the photoelectric electrons, and finally a sharp current pulse is output. The sharp current pulse is then selected and modulated by a SPEX DM102 discriminator to a rectangular pulse. In this data acquisition process, a threshold voltage is set. A voltage which is lower than this threshold would be considered as a noise current and be cut off from the recording.

2.3.5 Methods

To start the PL measurement on a sample, we first need to adjust the optical system. In this process, only the two mirrors right adjacent to the sample needed to be adjusted by rotating the screws on the back side of the mirrors with an aim to maximize the PL intensity. When the excitation light source was incident on the sample, the laser spot was usually slightly unfocused. The luminescence was emitted from the sample and collected by the collecting lens and focussed onto the entrance slit of the spectrometer. After collimation by a spherical mirror, the luminescence light was dispersed by the first grating into wavelength components. For different wavelength components, the diffraction angles are different. Thus, they are separated from each other in space. For the spectrograph in this work, a double gratings design is applied. The two gratings are connected in series with their mechanical systems operating in tandem, so that they both select the same wavelength. A double monochromator is used to reject the stray light. This can be very important when the laser line is close to the measured line (This is not really necessary in our case). By moving the gratings, different wavelength components are allowed to go through the spectrometer to reach the photocathode of the PMT. The resolution of this PL system is determined by the grating spacing and the widths of the entrance and exit slits. For example, when we closed the entrance and exit slits to 10 μm, the resolution was as high as 0.01 nm (0.06 meV) at 325.031 nm.

Chapter 3

Photoluminescence results

In this chapter photoluminescence (PL) data from epitaxial ZnO thin films grown on *c*-plane sapphire substrates by metalorganic chemical vapour deposition (MOCVD) are discussed. First a brief introduction to the theory of PL spectroscopy is presented. Intentional n-type doping of ZnO by MOCVD with group III dopants such as indium and aluminum at high growth temperature are discussed. Unambiguous observation of donor bound exciton emission from the indium dopant in the low temperature PL spectrum of In-doped ZnO allows us to identify shallow donors in these materials. The identification of shallow donors allows us to infer the residual compressive strain in the layers due to a lattice mismatch between ZnO and sapphire substrate. In order to investigate the effect of annealing on the PL emission, pre-growth annealing of the sapphire substrate and post-growth annealing of ZnO epilayers are discussed here. The low temperature PL transitions were also measured for ZnO samples grown at different temperatures.

3.1 Introduction

PL is a process in which a substance is excited to a higher energy state by photons and then drops back to a lower energy state accompanied by the emission of a photon. The energy of an emitted photon gives the energy separation of two electronic states in the material. The distribution of photon energies of the emitted light depends on the details of the band structure of the material. Impurity atoms in the material can also bring new energy levels into the band gap. Impurities which produce an electronic state close to the valence or

conduction band are called as shallow acceptors and shallow donors, respectively. PL is a powerful and sensitive optical method for detecting impurities and defects in the material. Those defects can strongly affect the material quality and device performance.

3.1.1 Theory of photoluminescence spectroscopy

Exciton

An exciton or electron-hole pair is a bound state of an electron and hole, which is formed by exciting an electron from the valence band into the conduction band by absorbing a photon to leave behind a positively charged hole. The electron is attracted to the hole by the electrostatic Coulomb force. The bound energy states of an exciton are analogous to those of an hydrogen atom. The physical process of a free exciton transition (FX) is shown in Fig. 3.1 (a). In this transition, the electron in the conduction band recombines with the hole and a photon is emitted. The total transition energy is given by:

$$E_{FX} = E_g - E_b \tag{3.1}$$

where E_g is the bandgap energy of a semiconductor and E_b corresponds to the binding energy of a free exciton. The free exciton binding energy can be estimated by the hydrogen atom model [22]:

$$E_b = \frac{m_r^* q^4}{8\varepsilon^2 \varepsilon_0^2 h^2} \tag{3.2}$$

where q is the elementary charge, ε_0 is the dielectric constant of free space, ε is the relative dielectric constant of ZnO, and h is Planck's constant. m_r^* is the effective mass of an exciton which can be obtained from Eqn. 3.3 [22]:

$$\frac{1}{m_r^*} = \frac{1}{m_e^*} + \frac{1}{m_h^*} \tag{3.3}$$

where m_e^* and m_h^* are the electron and hole effective masses, respectively. Figure 3.1 (b) shows the physical process of a neutral donor bound exciton transition (D^0X). In this transition, the exciton was initially bound to a neutral donor atom. Then the electron-hole pair recombined with a photon emitting and the donor atom remains in its $1s$ ground state. The total transition energy for a neutral donor bound exciton is given by:

$$E_{D^0X} = E_g - E_b - E_{loc} \tag{3.4}$$

where E_{loc} is the bound exciton localization energy which can be calculated by measuring the neutral donor bound exciton emission energy. The typical E_{loc} value is in the region 13-30 meV [23]. The physical process of an ionised donor bound exciton transition (D^+X) is shown in Fig. 3.1 (c). After formation of a free exciton, the electron-hole pair can also be captured by an ionised donor atom. This can only happen for certain effective mass ratios of electron to hole [24]. Figure 3.1 (d) shows the physical process of a two-electron satellite transition (TES). In this kind of transition, the exciton was initially bound to a neutral donor atom as for the D^0X transition. In the wake of the radiative recombination of the bound exciton, the donor atom is left in the $2s$ or $2p$ excited state. This reduces the photon energy compared with the D^0X process (Fig. 3.1 (b)). It also allows us to calculate the donor binding energy, which is equal to $4/3$ times of the energy separation between D^0X and TES transitions [23].

Donor-acceptor-pair transition

At very low temperatures, if both donor and acceptor impurities are present in the material, electrons and holes created by absorbing photons can be captured by ionised donors (D^+) and acceptors (A^-) to form neutral donors (D^0) and acceptors (A^0). The physical process of a donor-acceptor-pair transition (DAP) is shown in Fig. 3.1 (e). The total transition energy for a donor-acceptor pair is given by [25]:

$$E_{DAP} = E_g - E_A - E_D + \frac{e^2}{4\pi\varepsilon_0\varepsilon}\frac{1}{r} \tag{3.5}$$

where E_A and E_D are the acceptor and donor binding energies, respectively, ε_0 is the dielectric constant of free space, ε is the relative dielectric constant of ZnO and r is the average distance between occupied donor and acceptor centers. The last term on the right hand side of Eq. 3.5 represents the Coulomb interaction between the ionised donors and acceptors. We did not see clear evidence of DAP emission in our samples. This is most likely due to the fact that the donor concentration is much higher than the acceptor concentration.

Deep-level luminescence

Besides the shallow donors and acceptors we discussed previously, deep dopant atoms are also likely to be introduced into the material, for example, copper impurities, which create

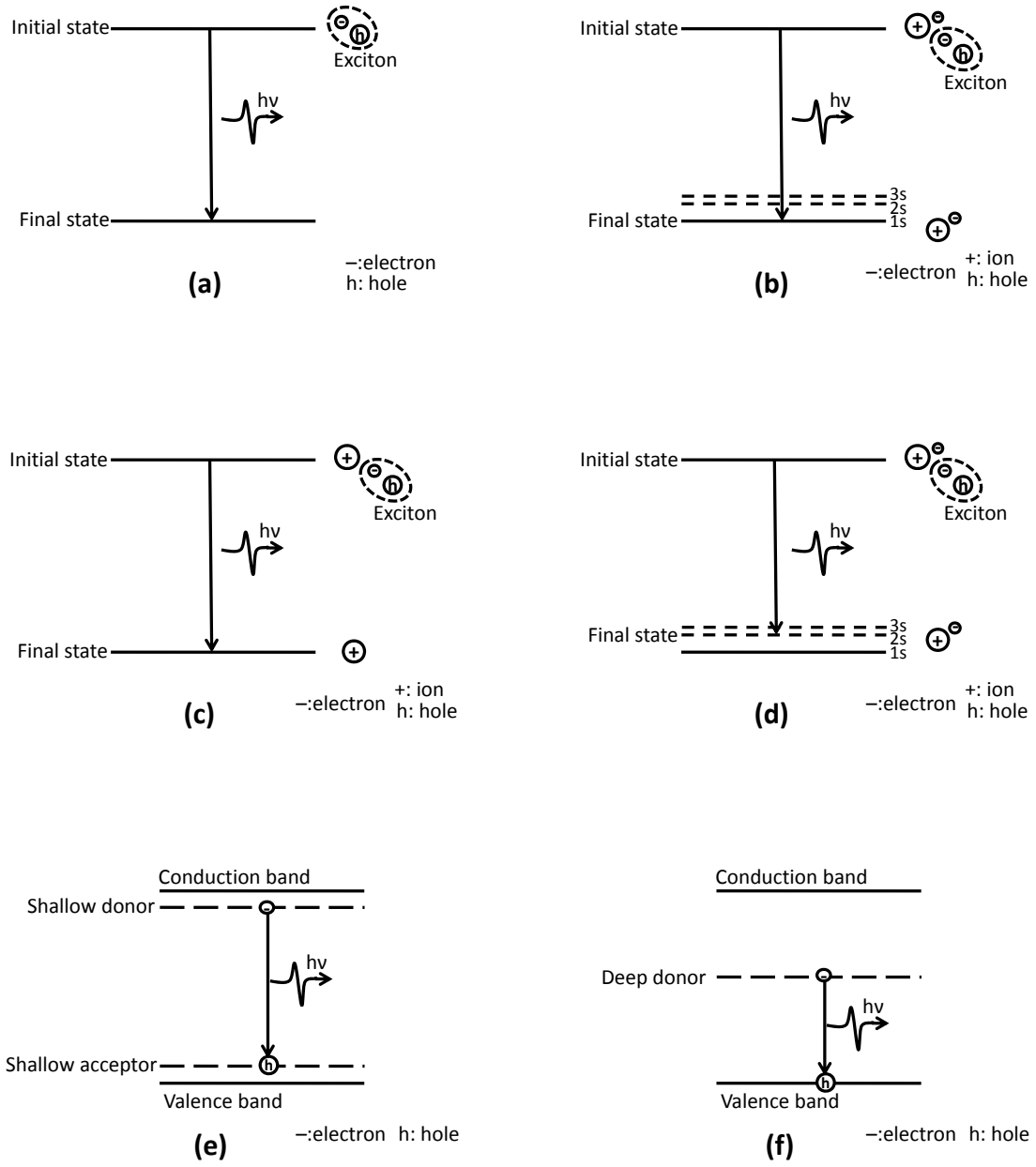

Figure 3.1: Schematic diagrams of the physical processes of various PL transitions, (a) free exciton recombination (b) neutral donor bound exciton recombination (c) ionised donor bound exciton recombination (d) two-electron satellite transition (e) donor-acceptor pair transition (f) deep-level luminescence.

electronic states close to the central position of the bandgap. Electrons can be excited to this state by absorbing photons to produce electron-hole pairs. When returning to equilibrium, the electron recombines and a photon is emitted which has an energy much lower than the bandgap. The physical process of this emission is presented in Fig. 3.1 (f).

Effective mass theory

In a semiconductor, the energy required to remove the extra electron from a shallow donor atom can be estimated based on a hydrogen-like model and the effective mass theory. The donor ionization energy is given by [22]:

$$E_D = \frac{m_e^* q^4}{8\varepsilon^2 \varepsilon_0^2 h^2} = \frac{m_e^*}{m_0 \varepsilon^2} E_H \tag{3.6}$$

where m_e^* is the effective mass of an electron in the periodic potential of ZnO, m_0 is the free electron mass, q is the elementary charge, ε_0 is the dielectric constant of free space, ε is the relative dielectric constant of the semiconductor, and h is Planck's constant. E_H is the ionization energy of the free hydrogen atom equal to 13.6 eV. For ZnO, the electron effective mass in the conduction band is given by $m_e^* = 0.252 m_0$ [26, 24] and the macroscopic relative dielectric constant $\varepsilon = 8.267$ [27, 24] is calculated using the density functional theory (DFT) linear response method. Therefore, the ionization energy for an ideal effective mass donor, measured from the conduction band edge, can be calculated from Eqn. 3.6 and is 50.15 meV.

Haynes' rule and central cell effect

Empirically researchers have observed a linear relationship between donor bound exciton localization energy E_{loc} and donor binding energies E_D. This is called Haynes' rule [28]:

$$E_{loc} = \alpha E_D \tag{3.7}$$

For ZnO, the proportionality constant is equal to 0.3 [23]. The experimental data on the exciton localization energies, the impurity binding energies, and the resulting ratios are shown in Table 3.1.

According to the effective mass theory, the donor binding energy in ZnO is equal to 50.2 meV. However, the experimental data listed in Table 3.1 show that the binding energies are varied with donor species. The difference in donor binding energies indicates

Table 3.1: Experimental data on the exciton localization energies E_{loc}, the impurity binding energies E_D, and the resulting ratios of E_{loc} to E_D. The data shown here are from Meyer et al. [23].

Donor	E_{loc} (meV)	E_D (meV)	E_{loc}/E_D
H	13.1	46.1	0.284
Al	15.1	51.6	0.293
Ga	16.1	54.6	0.295
In	19.2	63.2	0.304

the remarkable influence of the core electrons of the impurity donor on the binding energy, which is called the central cell effect. According to Haynes' rule, the localization energies for the excitons bound to different donors are varied. The resulting changes in E_{loc} can be used to identify the chemical nature of donors in ZnO.

3.1.2 A typical photoluminescence spectrum of ZnO

A typical 4.2 K low temperature PL spectrum of an epitaxial ZnO thin film grown on *c*-plane sapphire substrate by MOCVD is shown in Fig. 3.2. Two peaks located at 3357.93 meV and 3361.02 meV labeled D^0X are ascribed to neutral donor bound exciton transitions [23]. These two transitions are extremely narrow peaks with linewidths of 0.36 meV and 0.18 meV, respectively. However, peak positions for these two transitions do not strictly agree with any previously reported values from bulk ZnO samples. In addition, two peaks located at 3368.74 meV and 3372.96 meV labeled D^+X are interpreted as ionised donor bound exciton transitions [23], which are correlated with the two D^0X peaks. A free exciton emission at 3376.82 meV labeled FX is also observed in this figure [23]. A very sharp and strong line located around 3333 meV labelled Y-line has been ascribed to the transition of excitons bound to structural defects [23]. However, the details are still not clear. In this transition, the excited exciton is believed to be bound to a structural defect donor instead of a donor atom. Two groups of broad doublet peaks labelled TES in the figure are assigned to two-electron satellite transitions [23], which correspond to the two D^0X transitions. The zone

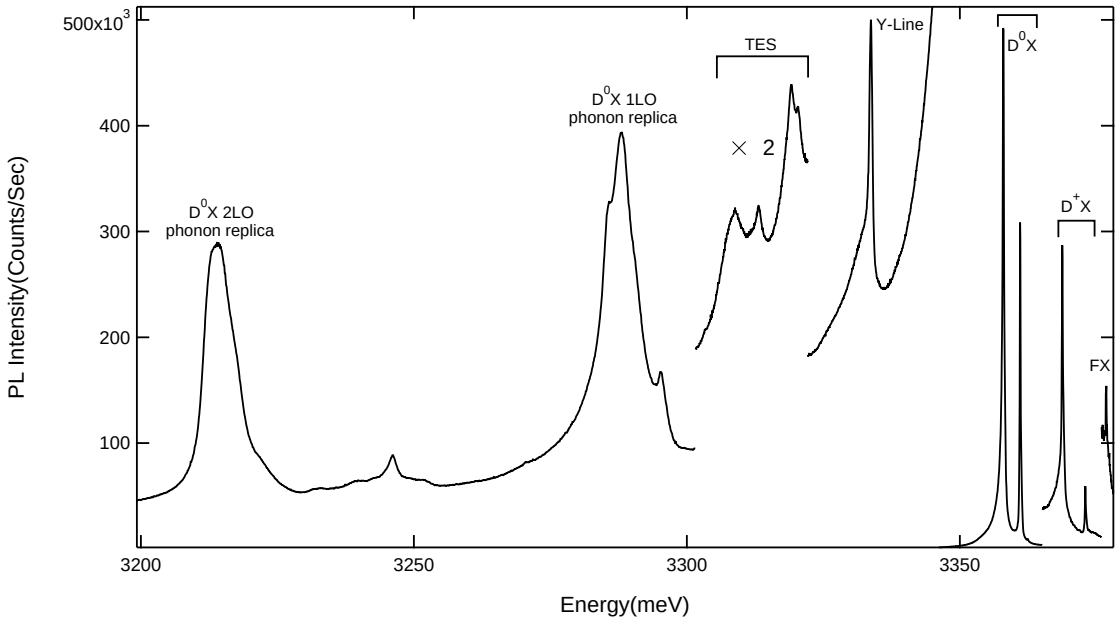

Figure 3.2: A typical 4.2 K low temperature photoluminescence spectrum of an epitaxial ZnO thin film grown on *c*-plane sapphire substrate by MOVPE, showing neutral donor bound exciton recombination, ionised donor bound exciton recombination, free exciton emission, two-electron satellite transition, and Y-line recombination. The corresponding phonon replica of the D^0X transitions with longitudinal optical phonons (LO) are also indicated. The widths of the entrance and exit slits of the spectrometer were narrower for the measurements between 3345 – 3380 meV (10 μm) than the measurements between 3199 – 3344 meV (100 μm). The peaks between 3365.1 meV and 3375.8 meV were blown up with a factor of 10, and the peak between 3375.9 meV and 3377.9 meV was blown up with a factor of 100.

centre longitudinal optical (LO) phonon energy $\hbar\omega_{LO}$ is equal to 72 meV for ZnO [29]. In the figure, we can assign the peaks between 3280 meV and 3300 meV to the first-order LO-phonon replica of donor bound exciton transitions. In addition, the peak at 3246.42 meV is due to a second-order LO-phonon replica of the D^0X transitions.

Photoluminescence in the deep level emission region

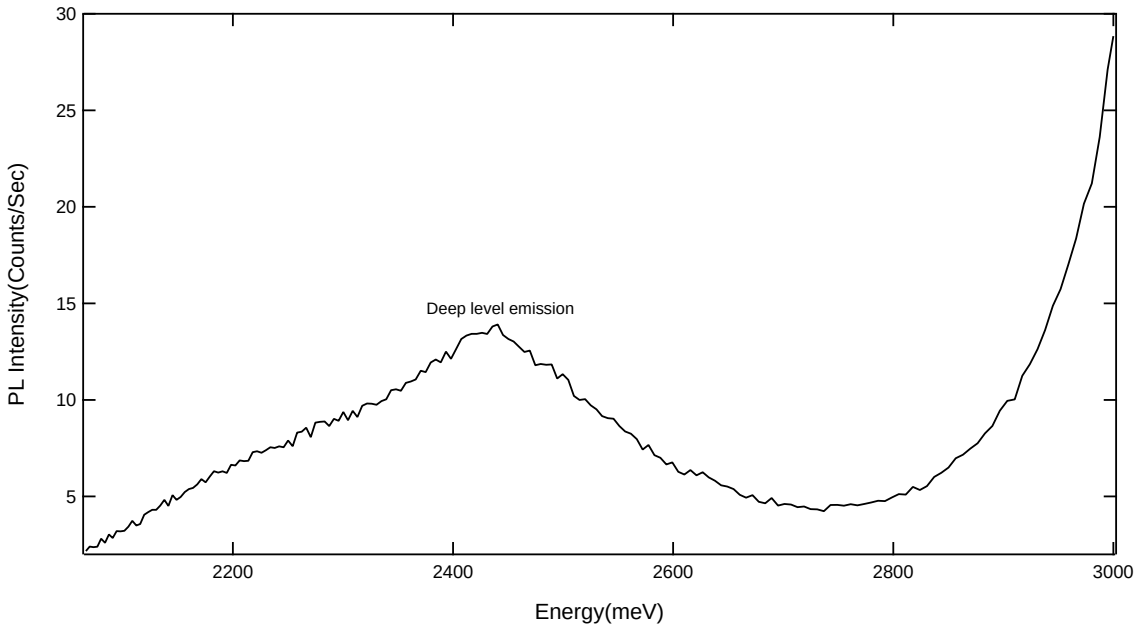

Figure 3.3: 4.2 K low temperature photoluminescence spectrum of an ZnO thin film grown on c-plane sapphire substrate by MOVPE, showing the deep level emission.

A 4.2 K low temperature PL spectrum of an epitaxial ZnO thin film in the deep level emission region is shown in Fig. 3.3. An extremely broad band centered around 2440.63 meV presented in the figure, which has a FWHM of about 200 meV. This transition has been assigned to a deep level emission - the green luminescence, which originates from movable intrinsic point defects such as oxygen vacancies (V_O) or zinc vacancies (V_{Zn}) in the ZnO thin film [29, 30]. It is necessary to point out that the green luminescence for our ZnO samples is very weak.

3.2 Identification of shallow donors by intentional indium doping

ZnO has a strong potential for short-wavelength optoelectronic device applications due to a wide bandgap of 3.37 eV at room temperature. To fulfill its great promise as an optoelectronic material, high quality n-type and p-type ZnO is required. Nominally undoped ZnO samples show intrinsic n-type conductivity with high electron concentration ($1.0 \times 10^{17} - 1.0 \times 10^{18}$ cm^{-3}) [31]. However, whether the donors are zinc interstitials (Zn_i) and oxygen vacancies (V_O), hydrogen donors, or shallow residual donors is still controversial. Intentional n-type doping can be attained by group III elements Al, Ga and In substituting for Zn sites, and group VII elements Cl and I substituting for O sites. Many groups have reported successful doping with Al, Ga and In, resulting in high conductivity n-type ZnO materials [32, 33, 34]. Group I elements Li, Na and K substituting for Zn sites, and group V elements N, P and As substituting for O sites have been investigated as p-type dopants [35]. However, controlled and uniform p-type doping in wide bandgap semiconductors such as ZnO is hard to realize. Some probable reasons were given in previous reports. Some researchers pointed out that the dopants are easily compensated by native defects such as Zn_i and V_O and H donors [17]. The low solubility of dopants in the host material also inhibits p-type doping [18]. Finally, the acceptor binding energies are large, leading to poor activation at room temperature.

Very few works on the identification of shallow donors in MOCVD grown ZnO have been done previously. Also there are almost no reports of intentional n-type doping of ZnO thin films by MOCVD, particularly at high growth temperatures where crystal quality is high enough to observe sharp excitonic PL. In order to identify the chemical nature of the D^0X transitions in the PL spectrum, intentional In doping of ZnO thin films was performed by MOCVD on *c*-plane sapphire substrates at 800°C. In the deposition process, dimethylzinc (DMZn) and nitrous oxide (N_2O) were used as the Zn and O precursors with a flow rate of 2.0 standard cubic centimeters per minute (sccm) and 3.0 standard liters per minute (slm), respectively. For the indium source we used trimethylindium (TMIn). Pure nitrogen was used as the carrier gas. The growth time was 1.0 hour and the ambient pressure was 700 Torr. Our primary characterization tool is low temperature photoluminescence (PL) spectroscopy.

3.2.1 Effect of In doping on the bound exciton transitions

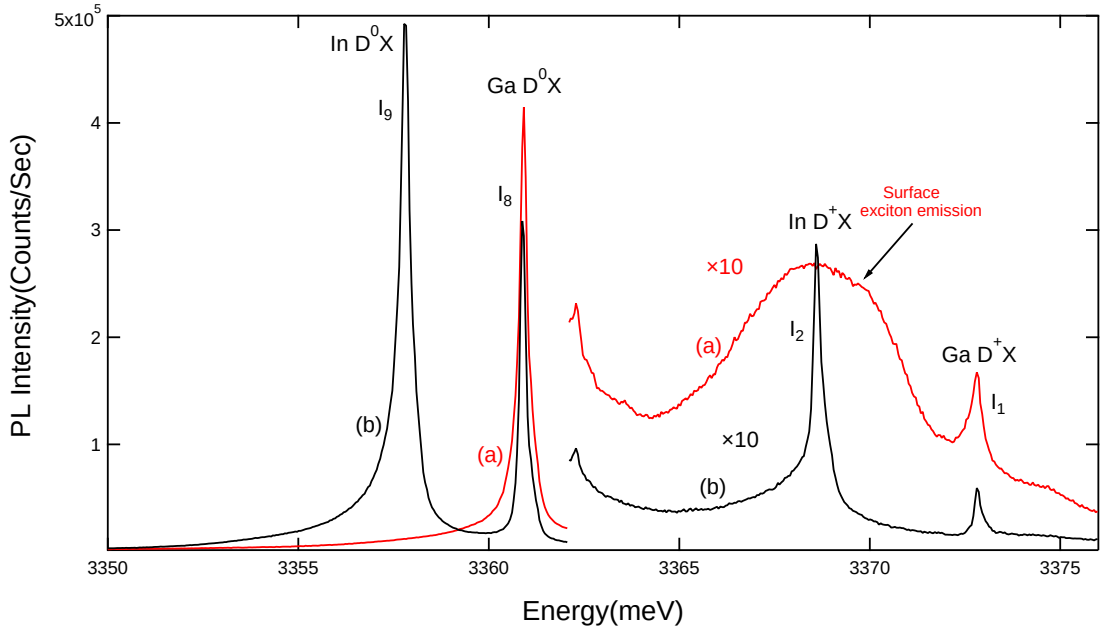

Figure 3.4: 4.2 K low temperature photoluminescence spectra of (a) undoped ZnO and (b) In-doped ZnO grown with 1.0 sccm TMIn flow.

Figure 3.4 (a) shows a typical 4.2 K low temperature PL spectrum of a nominally undoped MOVPE epitaxial ZnO thin film grown at 800°C using DMZn and N_2O. In this PL spectrum, two extremely sharp excitonic transitions located at 3360.92 meV and 3372.81 meV are clearly observed. The peak at 3360.92 meV is assigned to a D^0X transition, which has a linewidth of 0.19 meV. The line at 3372.81 meV is ascribed to a D^+X transition, whose full widths at half maximum (FWHM) is also small with a value of 0.32 meV. The energy, wavelength and linewidth values of the PL transitions appearing in this spectrum are listed in Table 3.2, to make a comparison with data from homoepitaxial ZnO material [23]. The linewidth of the D^0X transitions for our MOVPE grown ZnO epitaxial layer is much narrower than the values previously reported for most heteroepitaxial ZnO [36, 37, 38], but broader than the best reported homoepitaxial ZnO material (0.08 meV) [39]. Room temperature Hall measurements showed a residual electron concentration of 4.31×10^{17} cm^{-3} for this sample [31]. A broad peak located around

3368.41 meV with a linewidth of 4.02 meV is observed in the spectrum. The chemical origin of this line is not yet fully explained. However, some researchers believe that this line is due to the recombination of an exciton at the ZnO surface possibly at an adsorbed OH radical [40]. This peak is widely observed in the PL spectra of ZnO with a high surface to volume ratio (i.e. ZnO nanowires) [41, 42].

Table 3.2: The wavelengths and energies of the PL transitions in this work compared with data from homoepitaxial ZnO material. All the data were taken from the In-doped ZnO with an additional 1.0 sccm TMIn flow in the deposition process. Energy values of reference [23] were recalculated from their wavelength data using a conversion constant of 1239841 nm $\cdot$ meV between wavelength(nm) and energy(meV). I_1, I_2, I_8 and I_9 are labels commonly used in the ZnO PL literature.

PL transition	Energy This Work (meV)	Wavelength This Work (nm)	Energy Ref. [23] (meV)	Wavelength Ref. [23] (nm)	Blueshift (meV)	Linewidth (meV)
$Ga\ D^+X(I_1)$	3372.81	367.599	3371.79	367.71	1.02	0.32
$In\ D^+X(I_2)$	3368.59	368.060	3367.40	368.19	1.19	0.32
$Ga\ D^0X(I_8)$	3360.92	368.899	3359.73	369.03	1.19	0.19
$In\ D^0X(I_9)$	3357.78	369.244	3356.64	369.37	1.14	0.36

Figure 3.4 (b) shows a 4.2 K low temperature PL spectrum of an intentionally In-doped MOVPE grown ZnO thin film with a TMIn flow rate of 1.0 sccm during deposition. This In-doped ZnO was measured using the same spectrometer settings as the undoped sample in Fig. 3.4 (a). Besides the two lines located at 3360.92 meV and 3372.81 meV, two additional lines located at 3357.78 meV and 3368.59 meV appear in the PL spectrum of the In-doped ZnO. The thickness of the In-doped ZnO is 738 nm, which is very close to that of the undoped ZnO (768 nm). Atomic force microscopy (AFM) measurements indicate that the surface roughness of In-doped ZnO is 146 nm, and it is extremely close to that of the undoped sample (149 nm). We assign these two additional peaks at 3357.78 meV and 3368.59 meV to excitons bound to neutral and ionised indium donors and label them I_9 and I_2 as is usual in the ZnO PL literature. The group III element In is known to substitute for

Zn atoms and introduce shallow donor levels into the bandgap of ZnO. Secondary ion mass spectrometry (SIMS) measurements indicate an indium concentration of $\sim 8 \times 10^{18}$ cm^{-3} in the 1.0 sccm TMIn doped ZnO material. This SIMS data gives us strong evidence of successful In incorporation in the ZnO layers during deposition. The energy, wavelength and linewidth values of PL transitions appearing in this spectrum are listed in Table 3.2.

Table 3.2 shows a comparison between the data in this work and measurements from Meyer et al [23]. We find an average energy shift of 1.17 meV for the In-related D^0X and D^+X transitions for our In-doped ZnO epilayers compared with the values reported for bulk ZnO crystals and homoepitaxial ZnO material grown by MOVPE. At the deposition temperature of 800°C, the lattice constant of sapphire is $a = 4.78734$ Å, but the lattice constant of ZnO is $a = 3.26955$ Å [14]. For ZnO grown on a c-plane sapphire substrate, the lattice mismatch $(a_{ZnO} - a_{Sapphire})/a_{Sapphire}$ is -18% [8]. As a result, residual compressive strain is expected to exist in the ZnO thin film during growth. The residual compressive strain is able to result in an energy shift of the D^0X and D^+X transitions in the PL spectrum.

Table 3.2 shows that we get the best agreement by assuming that the lines at 3360.92 meV and 3372.81 meV are the I_8 and I_1 PL emissions which are known to be due to Ga neutral D^0X and Ga ionized D^+X transitions, respectively. With these assignments we get an similar blueshift of ~ 1.1 meV. The most likely source of the Ga is that it is a residual impurity in the DMZn organometallic source. Ga is a common byproduct of Zn metal refining. As a result, unintentional doping of the group III element-Ga during the deposition process of ZnO can not be avoided. Ga atoms can substitute for Zn atoms and behave as an n-type dopant. SIMS measurements indicate a residual Ga concentration of $\sim 4 \times 10^{16}$ cm^{-3} in the nominally undoped ZnO material. As we mentioned before, the electron concentration in undoped ZnO is 4.31×10^{17} cm^{-3}, which is much larger than the concentration of Ga. This indicates that the main contributions to the electron density in undoped ZnO material are native defects or surface donor states.

Hydrogen would seem to be unavoidable for MOVPE grown ZnO for the reason that hydrocarbon radicals take part in the chemical reaction. Due to its large mobility in the crystal lattice, hydrogen can easily diffuse into ZnO in large amounts. First-principles calculations suggested that isolated hydrogen at the bond-centered lattice site (H_{BC}) and hydrogen trapped within an oxygen vacancy (H_O) act as sources of the natural n-type conductivity and behave as shallow donors in ZnO [43, 44]. The excitonic recombination

of excitons bound to H_{BC} and H_O is expected to give rise to PL lines at 3360.1 meV and 3362.8 meV, respectively [45]. The absence of H_{BC} and H_O related D^0X transitions implies that hydrogen is not heavily incorporated into the ZnO layers. It is likely that hydrogen reacts very strongly at the surface with the N_2O oxygen source. This is an important result of our work, as previous authors have attributed the n-type conduction of ZnO to hydrogen donors [20, 46].

The electron concentration, as determined from a room temperature Hall measurement is equal to 9.8×10^{16} cm^{-3} for 1.0 sccm TMIn doped ZnO, which is much lower than the indium concentration of $\sim 8 \times 10^{18}$ cm^{-3} obtained from the SIMS measurement. The most likely explanation for this very low electron concentration is that most of In atoms are incorporated as complexes, are compensated by the native defects, or occur in separate In oxide phases.

3.2.2 Strain calculation

The most likely explanation for the observed blue shift in the In-related PL transitions is the presence of uniaxial tensile strain along the c axis ε_{cc}, in other words, biaxial compressive strain in the a plane ε_{aa}. The excitonic shift of the free exciton is approximated by evaluating the strain Hamiltonian including the first and second order terms. It is given by the following expression [47]:

$$\begin{aligned} \Delta E &= E(X_A) - E_A^0 \\ &= (D_1 - \frac{D_2}{\mu})\varepsilon_{cc} + a_+(D_3 - \frac{D_4}{\mu})\varepsilon_{cc} - \frac{a_+ a_-}{E_C^0 - E_A^0}[(D_3 - \frac{D_4}{\mu})\varepsilon_{cc}]^2 \end{aligned} \tag{3.8}$$

where ΔE represents the excitonic shift, $E(X_A)$ is the energy of the A free exciton in the strained ZnO and E_A^0 and E_C^0 are the energies of the free A and C excitons in unstrained ZnO. D_1, D_2, D_3 and D_4 are the deformation potentials. μ is the Poisson ration. a_+ and a_- are two expressions which are given by:

$$a_\pm = \frac{1}{2} \pm \frac{\Delta_1 - \Delta_2}{2\sqrt{(\Delta_1 - \Delta_2)^2 + 8\Delta_2^2}} \tag{3.9}$$

where Δ_1 is the crystal-field parameter, and Δ_2 is the spin-orbit splitting parameter.$E_A^0 =$ 3.3759 eV and $E_C^0 = 3.4199$ eV are the energy values of the free A and C excitons in

unstrained ZnO, respectively [47]. For ZnO, we use the values $D_1 = -3.90$ eV, $D_2 = -4.13$ eV, $D_3 = -1.15$ eV, $D_4 = 1.22$ eV, $\Delta_1 = 38.3$ and $\Delta_2 = 2.1$ [48]. The Poisson ration $\mu = \frac{C_{13}}{C_{33}}$. Here C_{13} and C_{33} are the elastic moduli. The average values for elastic constants in ZnO are $C_{13} = 105.6$ and $C_{33} = 210.2$ [49].

According to the values listed above, we can do the following calculations:

$$\begin{aligned} a_{\pm} &= \frac{1}{2} \pm \frac{\Delta_1 - \Delta_2}{2\sqrt{(\Delta_1 - \Delta_2)^2 + 8\Delta_2^2}} \\ &= \frac{1}{2} \pm \frac{38.3 - 2.1}{2\sqrt{(38.3 - 2.1)^2 + 8 \times 2.1^2}} \\ &= 0.5 \pm 0.49340 \end{aligned}$$

$$D_1 - \frac{D_2}{\mu} = D_1 - \frac{D_2}{\frac{C_{13}}{C_{33}}} = -3.9 - \frac{-4.13}{\frac{105.6}{210.2}} = 4.32089\ eV$$

$$D_3 - \frac{D_4}{\mu} = D_3 - \frac{D_4}{\frac{C_{13}}{C_{33}}} = -1.15 - \frac{1.22}{\frac{105.6}{210.2}} = -3.57845\ eV$$

Therefore, the excitonic shift can be expressed by Eqn. 3.10 for ZnO:

$$\Delta E = 0.76605\varepsilon_{cc} - 1.90741\varepsilon_{cc}^2 \tag{3.10}$$

with the relation $\varepsilon_{cc} = -2\frac{C_{13}}{C_{33}}\varepsilon_{aa}$ [47], the excitonic shift can be expressed as a function of the compressive strain in the a plane(ε_{aa}) as shown in Eqn. 3.11 for ZnO:

$$\Delta E = -0.76969\varepsilon_{aa} - 1.92560\varepsilon_{aa}^2 \tag{3.11}$$

We assume that the D^0X and D^+X transitions have a similar strain dependence as the free exciton transition. For the 1.0 sccm In-doped ZnO, the excitonic energy shift is equal to 1.165 meV. The residual strain that results in the blue shift in the 1.0 sccm In-doped ZnO can be obtained from Eqn. 3.11:

$$\begin{aligned} \Delta E &= -0.76969\varepsilon_{aa} - 1.92560\varepsilon_{aa}^2 \\ 1.165 \times 10^{-3} &= -0.76969\varepsilon_{aa} - 1.92560\varepsilon_{aa}^2 \\ \varepsilon_{aa} &= -1.52 \times 10^{-3} \end{aligned}$$

Strain from thermal expansion mismatch

For the 1.0 sccm In-doped ZnO discussed previously, the deposition process was performed at 800 °C. The ZnO sample was then cooled to room temperature and taken out of the reactor. During the low temperature PL measurements, the ZnO sample was cooled down to 4.2 K. As the thermal expansion coefficient of sapphire and ZnO are different from each other, this cooling process should induce compressive strain in the expitaxial layers. The lattice parameters of sapphire and ZnO single crystals at 800 °C and 4.2 K are listed in Table 3.3 [14].

Table 3.3: The lattice constants a and c of sapphire and ZnO single crystals at 4.2 K and 1073.15 K.

Material	Temperature(K)	a(Å)	c(Å)
ZnO	4.2	3.24819	5.20549
	1073.15	3.26955	5.22542
Sapphire	4.2	4.75590	12.97899
	1073.15	4.78734	13.07507

Assuming that ZnO thin films are fully relaxed at the growth temperature(800 °C), we can estimate the strain caused by thermal expansion mismatch during the cooling process from 800 °C to 4.2 K. For ZnO thin films grown on c-plane sapphire substrate, we assume that ZnO lattice expands at the same ratio with the underlying sapphire. Thus, we can derive the lattice parameter a of ZnO layers at 4.2 K from:

$$\begin{aligned} a_{ZnO/sample}|_{4.2\ K} &= a_{ZnO/relaxed}|_{1073.15\ K} \times \frac{a_{Sapphire}|_{4.2\ K}}{a_{Sapphire}|_{1073.15\ K}} \\ &= 3.26955 \times \frac{4.75590}{4.78734} = 3.24808\ \mathring{A} \end{aligned} \tag{3.12}$$

where $a_{ZnO/sample}|_{4.2\ K}$ is the lattice parameter a of ZnO layers at 4.2 K, $a_{ZnO/relaxed}|_{1073.15\ K}$ is the lattice parameter a of single crystal ZnO at 800 °C, $a_{Sapphire}|_{4.2\ K}$ is the lattice parameter a of single crystal sapphire at 4.2 K and $a_{Sapphire}|_{1073.15\ K}$ is the lattice parameter a of single crystal sapphire at 800 °C. Therefore, the compressive strain in the a plane resulting

from thermal expansion mismatch at 4.2 K is given by:

$$\begin{aligned} \varepsilon_{aa} &= \frac{a_{ZnO/sample}|_{4.2\ K} - a_{ZnO/relaxed}|_{4.2\ K}}{a_{ZnO/relaxed}|_{4.2\ K}} \\ &= \frac{3.24808 - 3.24819}{3.24819} = -3.39 \times 10^{-5} \end{aligned} \tag{3.13}$$

Conclusion

Our ZnO samples always show a 30° rotation of the crystal orientation of the ZnO epilayers against the sapphire substrate [8]. The ZnO lattice aligns itself according to the O atom sites. Therefore, the lattice mismatch is reduced from -31.7% to $\sim -18\%$ at 800 °C. The lattice mismatch will introduce a residual compressive strain into ZnO layers during growth. The compressive strain resulting from thermal expansion mismatch (3.39×10^{-5}) is much smaller than the strain existing in the 1.0 sccm In-doped ZnO (1.52×10^{-3}). Therefore, it is the lattice mismatch but not the thermal expansion mismatch that mainly results in the energy blueshift in the PL spectrum of the 1.0 sccm In-doped ZnO.

3.2.3 Effect of In doping on the two-electron satellite transition

Figure 3.5 (left side) shows 4.2 K low temperature PL spectra of a nominally undoped ZnO (a) and a 1.0 sccm In-doped ZnO (b) in the two-electron satellite region. Two adjacent broad lines located at 3319.14 meV and 3320.38 meV are observed for both the undoped ZnO and the In-doped ZnO. Two additional broad lines located at 3313.15 meV and 3308.82 meV appeared only in the PL spectrum of the In-doped ZnO. In a two-electron satellite transition, after recombination of the donor bound exciton, the donor atoms are left in the $2s$ or $2p$ excited states. Therefore, we should see doublet peaks in the TES region as shown in Fig. 3.5 (left side). The two adjacent lines at 3313.15 meV and 3308.82 meV can be assigned to In-related $2s$ state and $2p$ state TES transitions. As discussed previously, the dominant residual donor in the undoped ZnO is Ga. We assign the doublet lines at 3319.14 meV and 3320.38 meV to Ga-related two-electron-satellite transitions in the $2p$ and $2s$ states, respectively.

Figure 3.5 (right side) shows 4.2 K low temperature PL spectra of a nominally undoped ZnO (a) and a 1.0 sccm In-doped ZnO (b) in the excitonic transition region. The D^0X transitions are interpreted as neutral donor bound exciton emissions, leaving the donor atoms

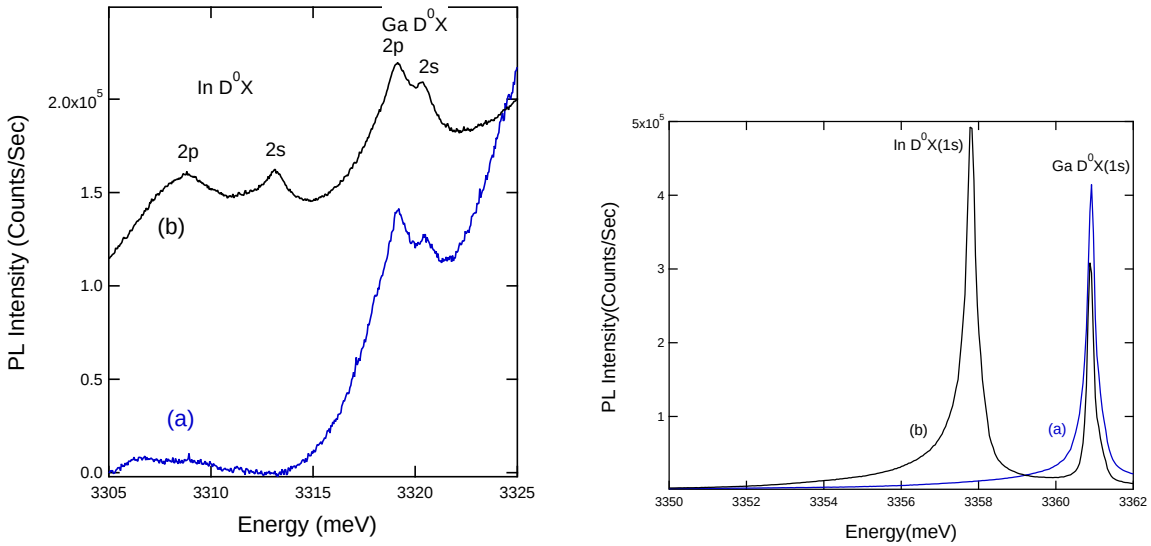

Figure 3.5: 4.2 K low temperature photoluminescence spectra in the bound exciton region of (a) a nominally undoped ZnO and (b) an In-doped ZnO grown with a TMIn flow rate of 1.0 sccm. The right side shows the excitonic region, and the left side shows the corresponding two-electron satellite region.

Table 3.4: The 1*s*-2*s* and 1*s*-2*p* energy separations for In and Ga dopants. The data in this work are taken from the In-doped ZnO with an additional 1.0 sccm TMIn flow in the deposition process. The data from reference [23] were estimated from the peak positions of relevant lines in the paper.

PL Transition	Energy Difference This Work (meV)	Energy Difference Reference [23] (meV)
In 1*s*-2*s*	44.63	44.7
In 1*s*-2*p*	49.14	48.7
Ga 1*s*-2*s*	40.54	40.3
Ga 1*s*-2*p*	41.78	41.8

in the ground state 1s. Therefore, we can obtain the 1s-2s and 1s-2p energy separations for In and Ga dopants, which are listed in Table 3.4. In the reference paper [23], the 1s-2s and 1s-2p energy separations were not reported directly. The reference data shown in Table 3.4 are estimated from their published PL spectra. The good agreement of the energy separations in our work with the values published in previous papers confirms our assignment about the chemical nature of the transitions in Fig. 3.5.

3.2.4 Temperature-dependent photoluminescence of In-doped ZnO

The temperature evolution of the PL spectrum for the 1.0 sccm In-doped ZnO was studied in detail in the near band edge region. The temperature dependent PL measurements were performed at temperatures between 4.2 K and 100 K, where most of the important changes took place. The temperature dependent PL measurements can also help to verify the chemical assignments of some of the peaks in the low temperature PL spectrum of the epitaxial ZnO thin films.

Figure 3.6 shows near band edge PL spectra for 1.0 sccm In-doped ZnO at different temperatures ranging from 4.2 K to 100 K. Increasing the temperature above 4.2 K results in the emergence of two additional lines, which shifts to higher energy from the In-related D^0X and Ga-related D^0X transitions by 4.51 meV. These are due to the spin-orbit splitting of the valence band into A (ground state) and B (first excited state) bands, which results in the formation of distinct A and B excitons. The A band excitons In $D^0X(A)$ and Ga $D^0X(A)$ decrease steadily with increasing the temperature. In contrast, the B band excitons In $D^0X(B)$ and Ga $D^0X(B)$ first increase with temperature reaching a maximum at 25 K, then decrease with increasing temperature and eventually vanish at temperatures above 80 K. The ionised donor bound exciton transitions In D^+X and Ga D^+X and the A free exciton emission FX_A decrease in intensity with increasing temperature, and finally vanish at temperatures above 25 K. As the temperature is increased, these three peaks start to converge due to the line broadening, which hampers an accurate determination of the peak positions.

From Fig. 3.6, we find that the peaks in the PL spectrum systematically shifted to lower energies with increasing temperature. This is due to the decrease in the band gap with increasing temperature. The transition energies obtained from the PL measurements are

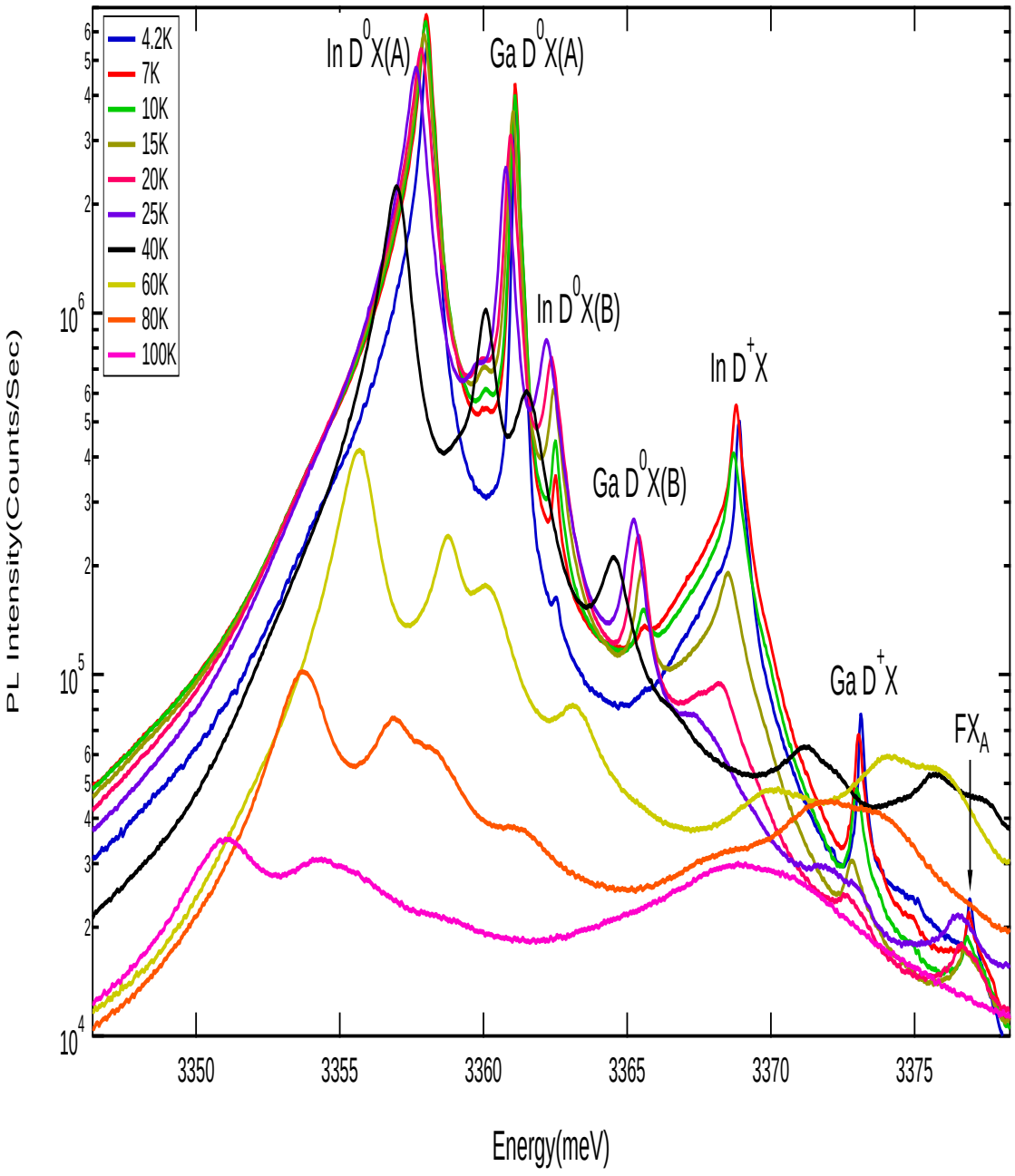

Figure 3.6: Evolution of photoluminescence spectrum as a function of temperature for 1.0 sccm In-doped ZnO in the near band edge region. Above 4.2 K, excitons associated with the B valence band emerge.

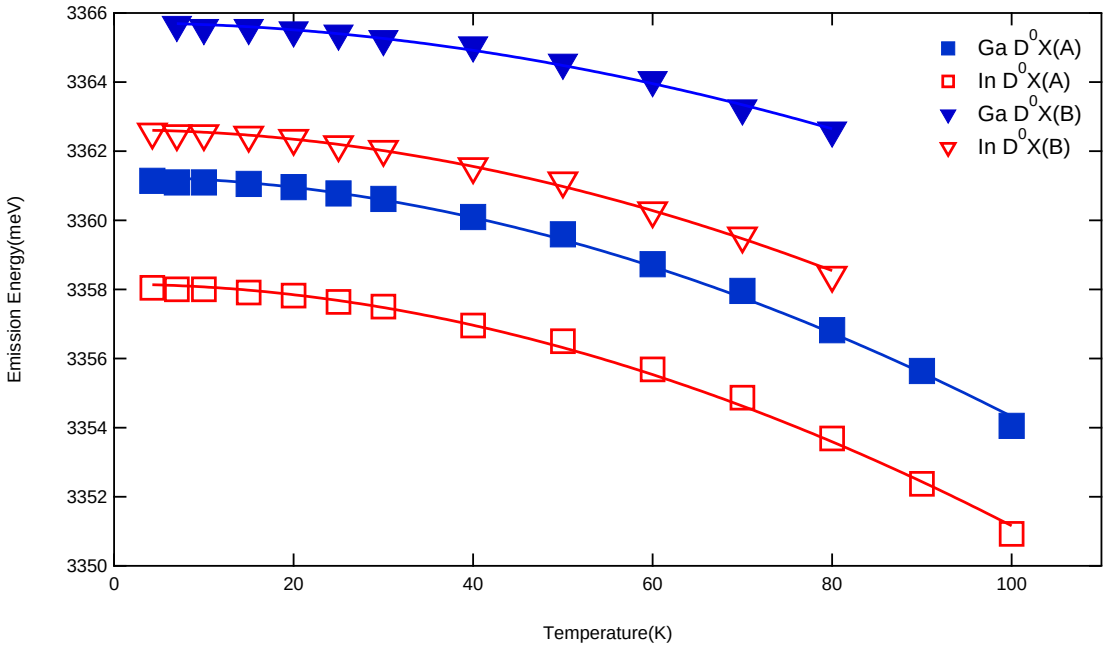

Figure 3.7: Temperature dependent peak positions obtained from (■) Ga-related A exciton D^0X, (□) In-related A exciton D^0X, (▼) Ga-related B exciton D^0X, (▽) In-related B exciton D^0X for the 1.0 sccm In-doped ZnO thin film measured at different temperatures from 4.2 K to 100 K. The experimental data were fitted using Varshni's empirical relation.

plotted in Fig. 3.7. Varshni's empirical formula can be used to analyze the experimental data [50, 51]:

$$E_g(T) = E_g(0) - \frac{\alpha T^2}{T+\beta} \tag{3.14}$$

where $E_g(0)$ and $E_g(T)$ are the band gap energy of ZnO at 0 K and T K, respectively, and α and β are Varshni's coefficients. The result of a linear least squares curve fitting is shown as the solid line in Fig. 3.7. During curve fittings, we fixed the parameter $\beta = 970\ K$, although previous authors reported various values for it [41, 52, 53]. We find that Varshni's empirical expression gives an adequate prediction of the peak positions of bound exciton transitions with increasing temperature.

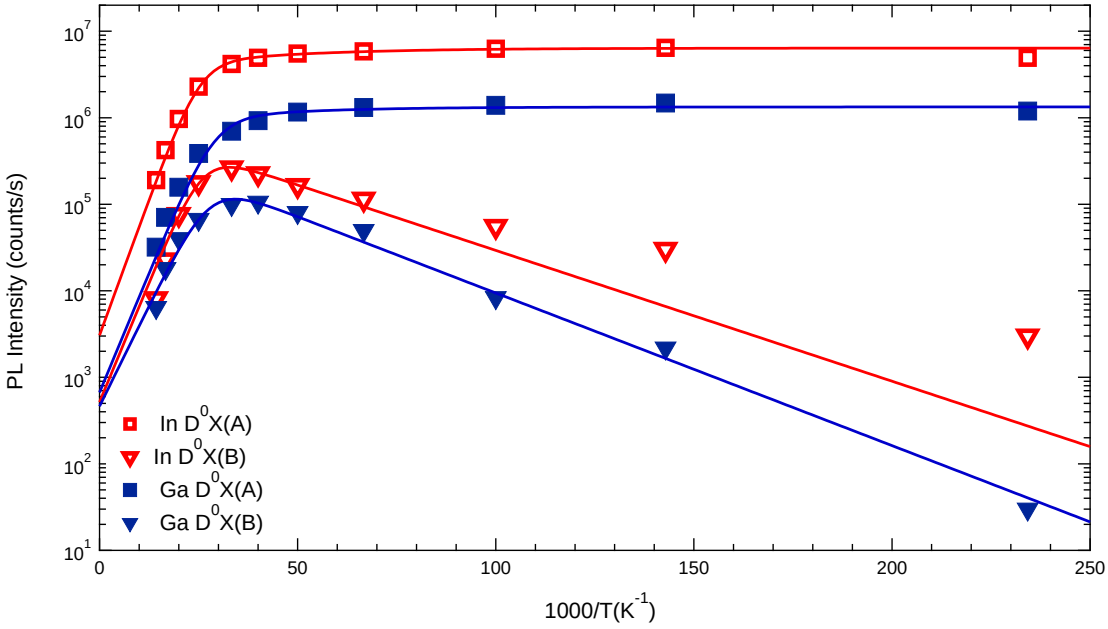

Figure 3.8: Temperature dependence of the integrated photoluminescence intensity for the Ga D^0X and In D^0X A and B exciton transitions. Solid lines represent fits using a simple Boltzmann model described in the text.

In Fig. 3.8, we show the integrated line intensity of the A and B excitons as a function of temperature. The solid lines in the figure represent fits based on a simplified model using

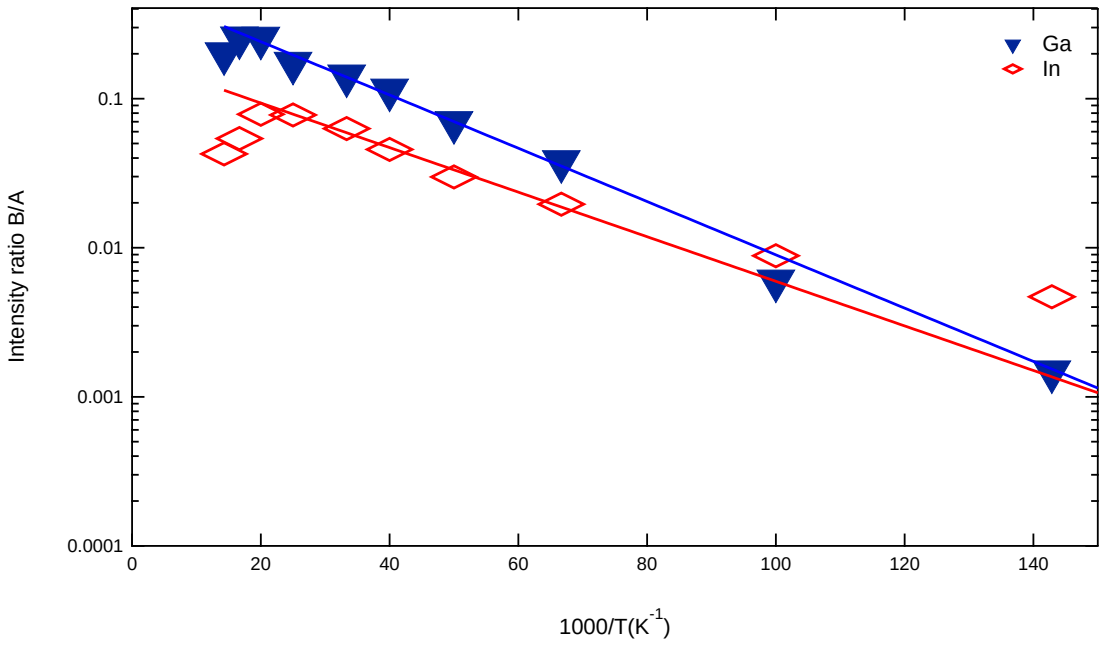

Figure 3.9: The integrated intensity ratio of the B exciton to the A exciton for Ga and In donors. The linear fits yield activation energies of 3.0 ± 0.2 meV and 3.5 ± 0.3 meV for In and Ga, respectively.

Boltzmann statistics for each type of donor atom. The A line intensity is fitted by:

$$I_A = \frac{I_0}{1 + \frac{g_B}{g_A} e^{-\frac{E_{AB}}{k_B T}} + \frac{g_X}{g_A} e^{-\frac{E_{DX}}{k_B T}}} \tag{3.15}$$

where g_A and g_B are the A and B bound exciton degeneracies, assumed equal, and of order one. g_x is the free exciton degeneracy, which is much larger than the bound exciton degeneracy and is used as a fitting parameter. E_{AB} is the A-B spin-orbit splitting of the valence band, which is measured to be 4.9 meV [23]. E_{DX} is the binding energy of the bound exciton relative to the transversal free A-exciton state. The B line intensity is fitted by:

$$I_B = \frac{I_0 e^{-\frac{E_{AB}}{k_B T}}}{1 + \frac{g_B}{g_A} e^{-\frac{E_{AB}}{k_B T}} + \frac{g_X}{g_A} e^{-\frac{E_{DX}+EAB}{k_B T}}} \tag{3.16}$$

Figure 3.9 shows the integrated intensity ratio of the B band exciton to the A band exciton for In and Ga donors together with linear fits over the range 10 K to 50 K. The activation energies calculated from the fitting are 3.0 ± 0.2 meV and 3.5 ± 0.3 meV for In and Ga, respectively. These values are lower than the spectroscopic splitting of 4.9 meV, which may be due to incomplete thermalization of the carriers at the lowest temperatures.

In order to obtain the best overall fit, only the degeneracy ratio g_X/g_A was used as an independent fitting parameter for each curve. The calculated values from Fig. 3.9 were used for E_{AB}, and 22 meV and 25 meV were set as the donor localization energies for the Ga D^0X and In D^0X lines, respectively. The fits show qualitative agreement with the experimental data. However, the assumption of thermal equilibrium is not really justified as we have neglected kinetic factors. The localization energies used for fits are larger than the accepted spectroscopic values of 16.1 meV and 19.2 meV. This may indicate the presence of additional nonradiative recombination channels. The discrepancy between the experimental data and the fitting curves may be due to systematic temperature errors.

3.2.5 Effect of In dopant concentration

In this section, a series of ZnO samples doped with different amounts of In precursor was investigated. The doping information is listed in Table 3.5. These ZnO samples were grown using DMZn and N_2O as the Zn and O precursors with flow rates of 2.0 sccm and 3.0 slm,

respectively. For each sample, the ZnO deposition process lasted for 60 minutes at 800 °C, at a pressure of 700 Torr. The doping efficiency of the In precursor and the electronic and optical properties of ZnO layers with different amounts of dopant were investigated. High resolution PL measurements were the primary characterization method used in this work.

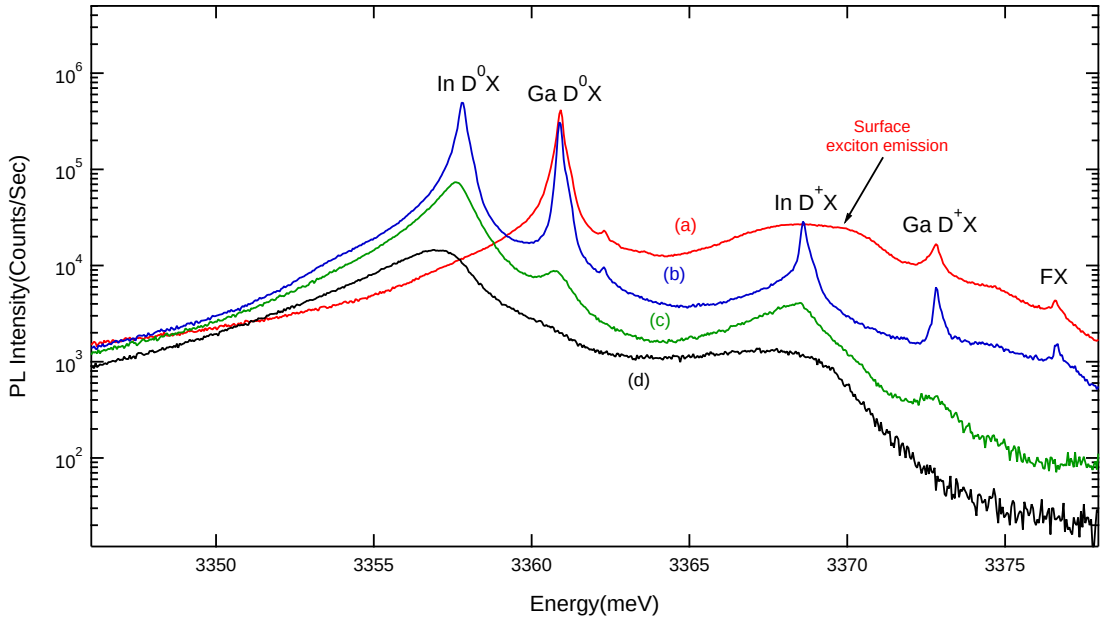

Figure 3.10: Effect of increasing In dopant concentration on 4.2 K low temperature PL lines. TMIn flow ranges are (a) 0 sccm, (b) 1.0 sccm, (c) 5.0 sccm and (d) 20.0 sccm.

Figure 3.10 shows 4.2 K low temperature PL spectra of ZnO thin films grown with different amounts of TMIn added during growth. Four samples were measured with the same spectrometer settings. In the spectra, the intensity ratio of In D^0X to Ga D^0X increases steadily with increasing TMIn flow, which is strong evidence of successful substitutional doping of indium into the ZnO layers. The linewidth of In D^0X also increases with the TMIn flow, which may imply an increased density of structural or point defects. It may also be due to a very high dopant concentration. In the figure, an overall intensity decrease of near band edge emissions is observed with increased In dopant concentration. This reduction in the PL intensity with increasing TMIn flow may also imply an increased density of structural or point defects, or a very high donor concentration.

Table 3.5: In dopant flow, layer thickness, surface roughness, In concentration, electron concentration of ZnO samples $H263$, $H265$, $H266$ and $H268$. The rocking curve widths of the ZnO (0002) diffraction peak for these samples are also shown here. The electron concentration data were obtained from room temperature Hall measurements [31]. The indium concentration data were acquired from SIMS measurements. The FWHM data were obtained from $\omega - 2\theta$ x-ray diffraction measurements. The RMS is the abbreviation of root mean square.

Sample Number	TMIn Flow Rate (sccm)	Layer Thickness (nm)	RMS Surface Roughness (AFM) (nm)	Electron Concentration (Hall) (cm^{-3})	Indium Concentration (SIMS) (cm^{-3})	FWHM (XRD) (°)
$H263$	0	768	149	4.31×10^{17}	1.0×10^{18}	0.183
$H266$	1.0	738	146	9.84×10^{16}	8.0×10^{18}	0.186
$H265$	5.0	721	104	2.53×10^{17}	7.0×10^{19}	0.247
$H268$	20.0	677	62.4	1.91×10^{17}	2.6×10^{20}	0.577

SIMS results listed in Table 3.5 show that the indium concentration increased with increasing TMIn flow rate, which indicates successful doping of indium into the ZnO layers during growth. However, SIMS can not tell where the In resides within the crystal lattice. The undoped material shows an In background doping with a concentration around 1.0×10^{18} atoms/cm^3 (which is probably the detection limit). Unfortunately, room temperature Hall measurements did not show a significant increase in the electron concentration as the TMIn flow rate was increased. Here the undoped sample is shown to have the highest electron concentration and the sample with 1.0 sccm TMIn has the lowest electron concentration. In addition, we find that the electron concentration is orders of magnitude smaller than the indium concentration for every sample as shown in Table 3.5. A most likely explanation for this phenomenon is that most of the indium atoms are incorporated as In clusters or secondary indium oxide phases, or are partially compensated by native or structural defects.

X-ray rocking curve measurements show a systematic increase in the full widths at half maximum of the ZnO (0002) diffraction peak from 0.183° to 0.577° as the TMIn flow rate increased from 0 to 20.0 sccm. This broadening also suggests an increased density of structural and point defects or secondary phases in the ZnO layers. It is hard to tell any difference in the morphology of these four samples. However, the atomic force microscopy (AFM) data in Table 3.5 shows that the surface of the ZnO layers becomes smoother with increasing TMIn flow. In addition, the growth rate decreases slightly as the In dopant concentration increases.

In summary, the PL spectra show the incorporation of some substitutional In into the ZnO layers, but this doping does not appear to affect the Hall results. Ben-Yaacov et al. also reported the use of TMIn for n-type doping of ZnO thin films grown by MOCVD recently [34]. They grew the ZnO:In samples at a higher temperature (950 °C) and observed a higher doping efficiency, however they also found poor activation of the In as electrically active donors.

3.3 Intentionally Al-doped ZnO

Intentional n-type doping by group III element In has been discussed in the previous section. Here controlled n-type doping by another group III element Al is investigated. The

electronic and optical properties of these doped ZnO samples are observed by high resolution low temperature PL measurements. Minami et al. investigated Al-doped ZnO thin films as an alternative to indium doped zinc oxide for transparent conductive electrodes [54].

3.3.1 Effect of Al doping on the bound exciton transitions

Nominally undoped ZnO and Al-doped ZnO were grown by MOCVD on *c*-plane sapphire substrates at 800 °C. DMZn and N_2O were used as the Zn and O precursors with a flow rate of 2.0 sccm and 3.0 slm , respectively. For the aluminum source we used trimethylamine alane (TMAA, $AlH_3N(CH_3)_3$). This precursor has a low vapor pressure of $\sim$ 2 Torr at 25 °C, making it potentially ideal as a dopant source for MOCVD. Pure nitrogen was used as the carrier gas. The growth time was 60 minutes and the pressure was 700 Torr.

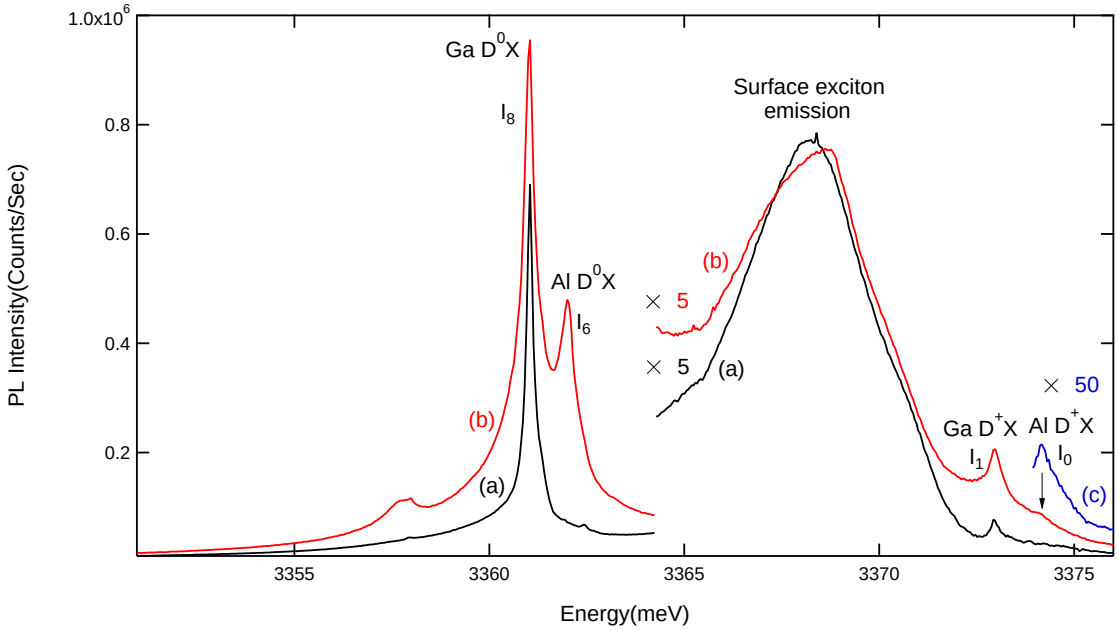

Figure 3.11: 4.2 K low temperature photoluminescence spectra of (a) undoped ZnO, (b) Al-doped ZnO grown with 5.0 sccm TMAA flow and (c) Al-doped ZnO grown with 10.0 sccm TMAA flow.

Figure 3.11 (a) shows a typical 4.2 K low temperature PL spectrum of nominally un-

doped ZnO. In the figure, two sharp lines located at 3361.04 meV and 3372.93 meV are observed in the spectrum. The linewidths of these two peaks are 0.23 meV and 0.32 meV. As we identified previously, these two transitions I_8 and I_1 are due to excitons bound to neutral and ionised Ga donors and labelled Ga D^0X and Ga D^+X. Figure 3.11 (b) shows a 4.2 K low temperature PL spectrum for an epitaxial ZnO thin film grown with an additional 5.0 sccm TMAA flow. In the spectrum, an additional sharp line located at 3362.00 meV is observed in addition to Ga D^0X and Ga D^+X, which has a linewidth of 0.27 meV. Another additional weak peak occurs at 3374.17 meV. This peak appears more strongly in the PL spectrum for ZnO grown with 10.0 sccm TMAA flow, which has a linewidth of 0.37 meV as shown in Figure 3.11 (c). We assign the transitions located at 3362.00 meV and 3374.17 meV to the I_6 and I_0 lines which are known to be due to recombination of excitons bound to neutral Al donor and ionised Al donor, respectively. These two peaks are labelled Al D^0X and Al D^+X. Surface exciton emission is observed in each spectrum located around 3368.26 meV with a linewidth of 4.16 meV.

Table 3.6: The wavelengths and energies of the PL transitions in this work compared with data from homoepitaxial ZnO materials. All the data were taken from the Al-doped ZnO using 5.0 sccm TMIn flow, except for I_0 which is obtained from ZnO with 10.0 sccm TMAA flow. Energy values of reference [23] were recalculated from their wavelength data using a conversion constant of 1239841 nm $\cdot$ meV between the wavelength(nm) and energy(meV). I_0, I_1, I_6 and I_8 are labels commonly used in the ZnO PL literature.

PL transition	Energy This Work (meV)	Wavelength This Work (nm)	Energy Ref. [23] (meV)	Wavelength Ref. [23] (nm)	Blueshift (meV)	Linewidth (meV)
$Al\ D^+X(I_0)$	3374.17	367.451	3372.75	367.63	1.42	0.37
$Ga\ D^+X(I_1)$	3372.93	367.586	3371.79	367.71	1.14	0.32
$Al\ D^0X(I_6)$	3362.00	368.781	3360.73	368.92	1.27	0.27
$Ga\ D^0X(I_8)$	3361.04	368.886	3359.73	369.03	1.31	0.23

The appearance of Al-related D^0X (I_6) and D^+X (I_0) suggests successful Al doping by MOCVD in this work and indicates that aluminum can act as a substitutional element for

Zn sites and introduce an additional shallow donor level into the bandgap of ZnO. Table 3.6 shows the energy, wavelength and linewidth data of PL transitions appeared in Fig. 3.11. From this table, we find an average energy shift of 1.345 meV for the Al-related D^0X and D^+X transitions for our 5.0 sccm Al-doped ZnO compared with the values reported for bulk ZnO crystal and homoepitaxial ZnO material grown by MOCVD. This is somewhat larger than the observed shift of 1.225 meV observed for the peaks Ga D^0X and Ga D^+X for the same sample.

Because the Y-line located at 3333 meV is very strong and broad, it is hard to distinguish the Al-related TES transitions from the PL spectrum (the Y-line overlaps the region where the Al-related TES transitions are expected to appear). Therefore, we did not observe any TES transitions in these samples.

3.3.2 Effect of Al dopant concentration

To investigate the doping efficiency of Al dopant (TMAA) and electronic and optical properties of Al-doped ZnO with different doping levels, a series of ZnO samples were grown by MOCVD on *c*-plane sapphire substrates using DMZn and N_2O as the Zn and O precursors with flow rates of 2.0 sccm and 3.0 slm, respectively. The addition of controlled amounts of Al precursor (TMAA) in the deposition process was performed. The doping information is listed in Table 3.7. For each sample, the ZnO growth time was 60 minutes at 800 °C at a pressure of 700 Torr.

Figure 3.12 shows 4.2 K low temperature PL spectra of ZnO thin films grown with different amounts of TMAA. Five samples were measured with the same spectrometer settings. In the figure, the intensity ratio of Al D^0X to Ga D^0X increases steadily as the TMAA flow rate increases from 0 sccm to 10.0 sccm, and the Ga-related donor bound exciton transitions Ga D^0X and Ga D^+X completely disappear when the TMAA flow rate is raised to 20.0 sccm and 50.0 sccm. This is strong evidence of successful doping of aluminum into the ZnO layers. The linewidth of the Al-related D^0X transition increases steadily with increasing TMAA flow, similar to the case for TMIn. The sample grown with 5.0 sccm TMAA displays the strongest overall PL intensity, but the Al-related D^+X transition which corresponds to Al D^0X is not obvious in the spectrum. The Al D^+X transition only appears in the spectrum for ZnO doped with 10.0 sccm TMAA. Increasing

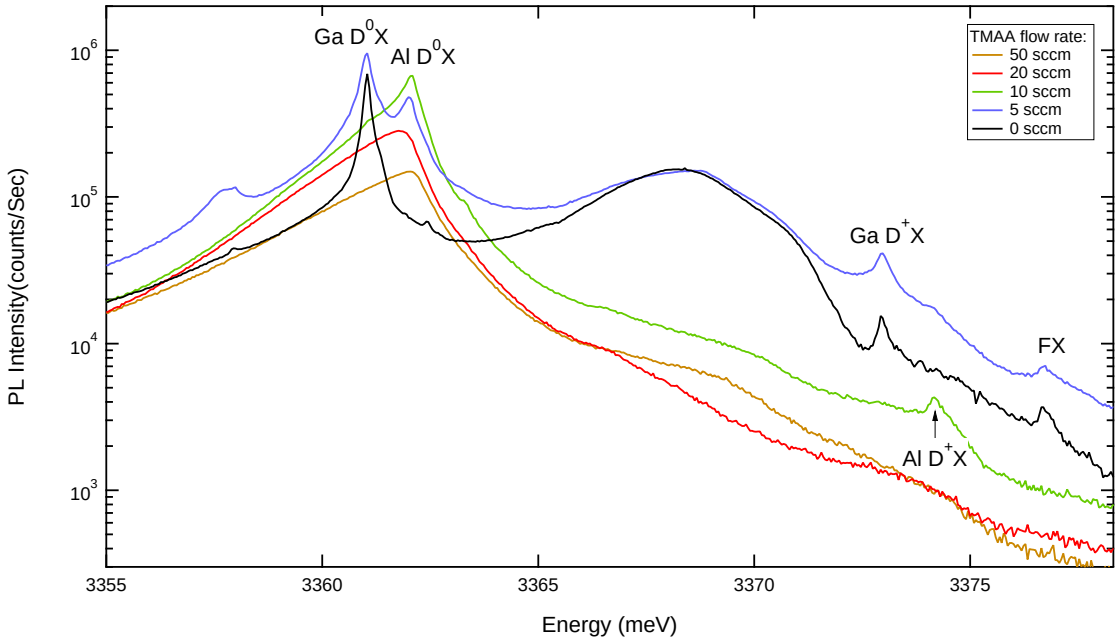

Figure 3.12: Effect of increasing Al dopant concentration on 4.2 K low temperature photoluminescence emission lines. TMAA flow rate ranges from 0 sccm to 50.0 sccm.

Table 3.7: Al dopant flow, layer thickness and surface roughness of ZnO samples $H314$, $H316$, $H317$, $H318$ and $H319$. The rocking curve widths of the ZnO (0002) diffraction peak for these samples are also showed here. The electron concentration data were obtained from room temperature Hall measurements [31] on a different series of samples, which were grown in the same conditions but on acetone cleaned and pre-annealed sapphire substrates. The FWHM data were obtained from $\omega - 2\theta$ x-ray diffraction measurements.

Sample Number	TMAA Flow Rate (sccm)	Layer Thickness (nm)	RMS surface roughness (AFM) (nm)	Electron Concentration (Hall) (cm^{-3})	FWHM (XRD) (°)
$H314$	0	640	135	8.29×10^{16}	n/a
$H316$	5.0	620	107	1.85×10^{17}	0.204
$H317$	10.0	573	79	1.90×10^{17}	0.201
$H318$	20.0	530	56	6.50×10^{17}	0.251
$H319$	50.0	231	n/a	n/a	0.266

the dopant concentration to 20.0 sccm and 50.0 sccm results in the complete removal of the Al D^+X transition. There is an overall intensity decrease of all the bound exciton emissions when the TMAA flow rate increases from 5.0 sccm to 50.0 sccm, similar to the case of indium doping.

The ZnO layer thickness decreases strongly with increasing TMAA flow. The sample grown with an additional 50.0 sccm TMAA has an extremely low growth rate. This significant drop in growth rate may indicate that TMAA has a parasitic reaction with DMZn. The chemistry of this process is not yet clear. The thin film surfaces show a large variation according to the AFM data shown in Table 3.7. The ZnO surface becomes more and more smooth with increasing the TMAA flow. The drop in surface roughness is probably due to the decreasing thickness of the ZnO layers. The XRD results listed in Table 3.7 show that the sample grown with 5.0 sccm TMAA has a similar rocking curve width of the ZnO (0002) diffraction peak compared with the sample grown with 10.0 sccm TMAA, and the samples with TMAA flow of 20.0 sccm and 50.0 sccm have a slightly higher FWHM value. The effect is much smaller than the case of TMIn doping. This indicates that the formation of secondary phases is much less pronounced for Al-doping than for In-doping. The room temperature Hall data show a small increase in the electron concentration with doping. However, the increase is much lower than expected based on the PL results. Further work is needed to understand the poor electrical activation of Al.

3.4 Effect of growth temperature on the optical properties of ZnO

The material properties of MOVPE grown ZnO thin films can be affected by various growth conditions. In this section, we discuss the effect of growth temperature on the PL properties of ZnO material. To investigate the effect of growth temperature, a series of ZnO samples were grown by MOVPE on *c*-plane sapphire substrates using DMZn and N_2O as the Zn and O precursors with flow rates of 2.0 sccm and 3.0 slm, respectively. For each sample, the ZnO growth time was 30 minutes and the ambient pressure was 700 Torr. The growth temperature information is listed in Table 3.8.

When the growth temperature is lower than 600 °C, the MOVPE grown ZnO thin films

Table 3.8: Growth temperature, layer thickness and surface roughness of various ZnO thin films: $H222$, $H229$, $H230$ and $H231$. For the AFM data, a range means that measurements were undertaken on different spots.

Sample Number	Growth Temperature (°C)	Thickness (nm)	AFM RMS (nm)
$H222$	800	410	$44-63$
$H229$	700	n/a	73
$H230$	600	455	76
$H231$	500	371	$38-45$

have a dark color and shiny surface. The samples become white and dull when the growth temperature is increased above 600 °C. We believe this is due to the presence of carbon nanoparticles. This will be discussed in more detail in Chapter 4. As shown in Table 3.8, there is no simple trend for the surface roughness and growth rate of the ZnO thin film as the growth temperature is increased. The samples grown at 500 °C and 800 °C seem to have a much smoother surface than the samples grown at 600 °C and 700 °C. The samples grown at 600 °C and 700 °C tend to have more rod shaped morphology based on SEM and AFM measurements.

Figure 3.13 shows 4.2 K low temperature PL spectra for ZnO thin films grown on *c*-plane sapphire substrates with different growth temperatures. The slit widths of the entrance and exit slits of the spectrometer were opened wider for the sample grown at 500 °C (100 μm) than other samples (50 μm) due to the weak PL emission. There is an overall intensity increase of near band edge emission as the growth temperature increases from 500 °C to 700 °C. The PL transitions in the spectrum of 800 °C ZnO appear to be pretty broad, which is quite different from the PL features shown in Fig. 3.4 (where the samples were grown for 1.0 hour). This is probably due to the reduction in strain for thicker layers. The big increase in intensity indicates a reduction in crystal point defects with increasing growth temperature. Besides the enhancement of the emission intensity, sharp line luminescence features due to D^0X and D^+X transitions related to Ga donors are present at 700 °C and 800 °C. This implies the existence of high quality ZnO with uniform or low strain. The higher intensity of the Y-line transition at 700 °C than 800 °C is interesting. ZnO layers

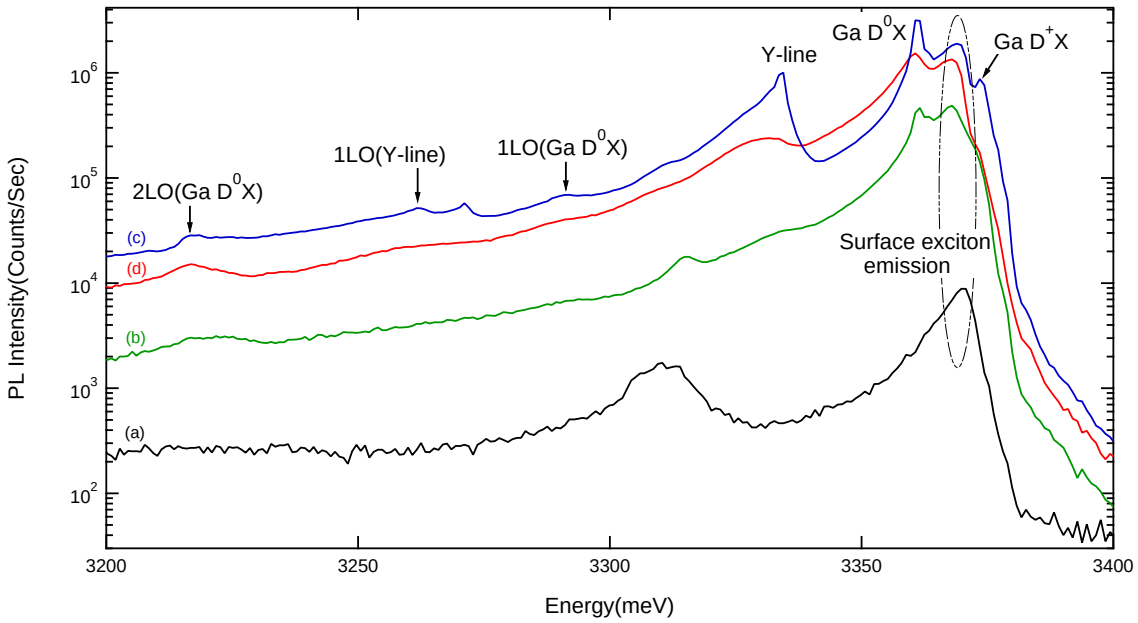

Figure 3.13: Effect of growth temperature on 4.2 K low temperature photoluminescence spectra for MOVPE grown ZnO thin films. Growth temperature ranges were (a) 500 °C, (b) 600 °C, (c) 700 °C, and (d) 800 °C.

grown at 700 °C exhibited a nanorod morphology. We have observed a high intensity of the Y-line in samples with nanorod morphology. Further work is required to confirm this observation.

In summary, ZnO thin films grown at higher growth temperatures such as 700 °C and 800 °C have a much better crystal quality and exhibit much better optical properties. Therefore, this project is focussed on the ZnO thin films grown at 800 °C.

3.5 Effect of annealing on the optical properties of ZnO

In this section, we investigate the effect of sapphire substrate pregrowth treatment and ZnO epilayer postgrowth annealing on the properties of the ZnO PL. Two methods of pregrowth treatment were investigated: one is cleaning in acetone and the other is annealing at 1100 °C in a tube furnace for 30 minutes with pure oxygen at a flow rate of 100 sccm. High temperature substrate annealing can reduce surface damage caused by crystal polishing. At high temperatures, surface atoms in the damaged regions can become mobile and form a better quality crystal lattice near the surface. Postgrowth ZnO samples annealing is usually performed at a temperature higher than the growth temperature and under pure oxygen, which can remove the carbon-related defects and prevent the loss of O in ZnO lattice (the Zn-O bond is easily broken at high temperatures).

3.5.1 Effect of pre-growth substrate annealing

To investigate the effect of pre-growth cleaning and annealing of the sapphire substrate on the structural and optical properties of ZnO, ZnO epilayers were fabricated on as-received, cleaned, and both cleaned and annealed sapphire substrates as shown in Table 3.9. The AFM images shown in Dichen Li's thesis indicate that the pre-growth annealing can result in a large improvement in the surface quality of the sapphire substrate. After annealing at 1100 °C, polishing scratches and polishing compound particles were removed, and atomic steps became evident on the surface. In this work, a series of ZnO samples were grown by MOCVD using DMZn and N_2O as the Zn and O precursors with flow rates of 2.0 sccm and 3.0 slm, respectively. For each sample, the growth time was 60 minutes at 800 °C at a pressure of 700 Torr.

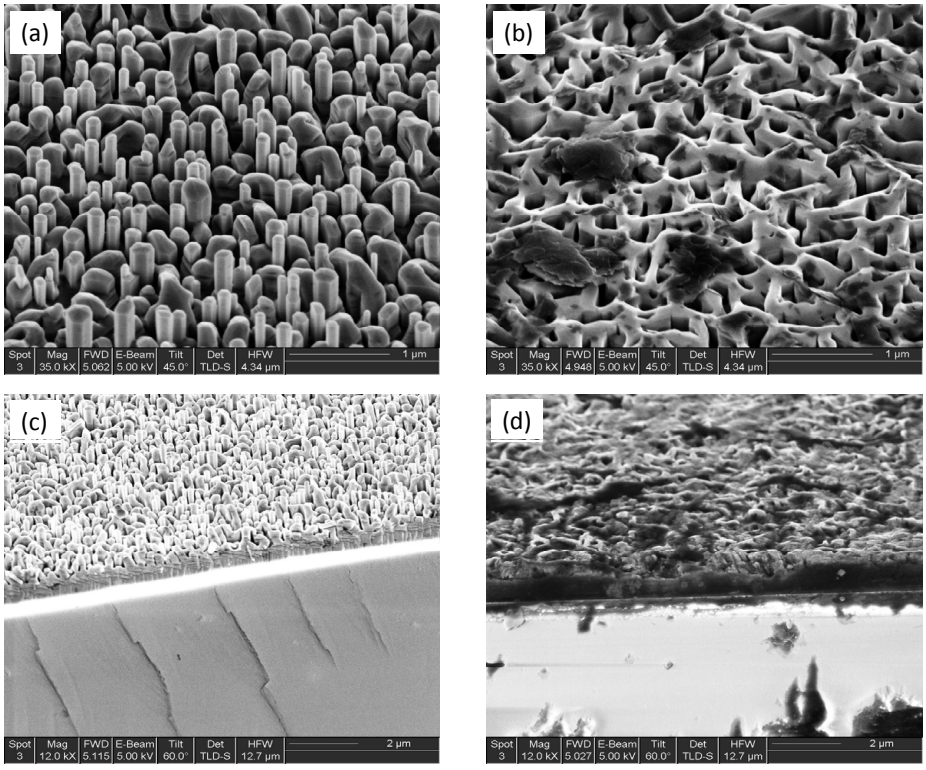

Figure 3.14: SEM images taken at 45° and 60° tilt angles of nominally undoped ZnO grown on (a) and (c) as-received sapphire substrates (b) and (d) sapphire substrates cleaned in acetone, and then annealed at 1100 °C in a tube furnace for 30 minutes with pure oxygen at a flow rate of 100 sccm. The SEM data were provided by Thomas Wintschel.

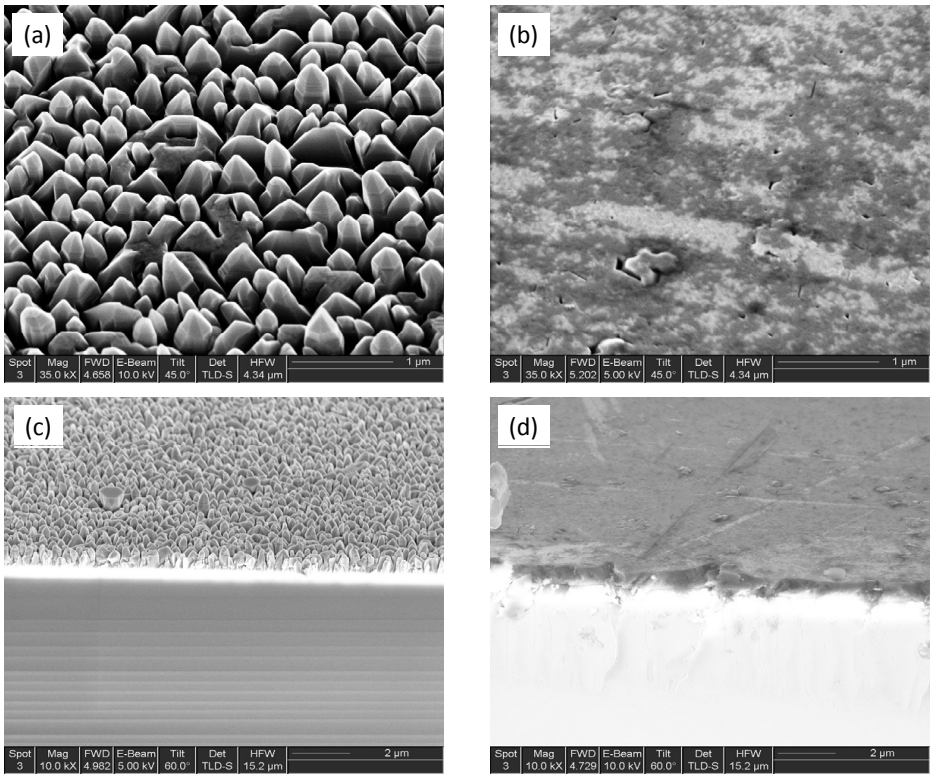

Figure 3.15: SEM images taken at 45° and 60° tilt angles of 5.0 sccm In-doped ZnO grown on (a) and (c) as-received sapphire substrates (b) and (d) sapphire substrates cleaned in acetone, and then annealed at 1100 °C in a tube furnace for 30 minutes with pure oxygen at a flow rate of 100 sccm. The SEM data were provided by Thomas Wintschel.

Table 3.9: Pre-growth substrate treatment, layer thickness and surface roughness of ZnO samples *H*269, *H*275 and *H*276.

Sample Number	Pre-growth treatment	Thickness (nm)	AFM RMS (nm)
*H*269	as received	829	96
*H*276	cleaned in acetone	715	51
*H*275	cleaned in acetone, and then annealed at 1100°C in a tube furnace for 30 minutes with pure O_2 at a flow rate of 100 sccm	743	33

Figure 3.14 shows scanning electron microscope (SEM) images of nominally undoped ZnO grown by MOCVD on (a) and (c) as-received sapphire substrates (b) and (d) sapphire substrates cleaned in acetone, and then annealed at 1100 °C in a tube furnace for 30 minutes with pure oxygen at a flow rate of 100 sccm. One-dimensional nanorods are clearly observed for the sample grown on as-received sapphire substrate; but for the material grown on the pre-treated sapphire substrate, a more interconnected net structure is formed. Figure 3.15 shows SEM images of 5.0 sccm In-doped ZnO grown on sapphire substrates with the above conditions. ZnO cones are distributed on the as-received sapphire substrate. Uniform planar thin films were formed on the pre-treated sapphire substrates. The SEM images show two interesting effects: one is that cleaner surfaces result in more two-dimensional lateral growth; the other is that the presence of In acts to provide an additional smoothing effect.

Figure 3.16 shows 4.2 K low temperature PL spectra of ZnO epilayers grown on (a) as-received, (b) cleaned, and (c) both cleaned and annealed sapphire substrates. These three samples were measured with the same spectrometer settings. For the ZnO grown on the as-received sapphire substrate, In-related donor bound exciton transitions In D^0X (with a linewidth of 0.64 meV) and In D^+X (with a linewidth of 0.32 meV), and Ga-related donor bound exciton transitions Ga D^0X (with a linewidth of 0.36 meV) and Ga D^+X (with a linewidth of 0.27 meV) are observed with high peak intensity. The In-related PL features originate from a memory effect from previous In doping experiments. For the epilayer

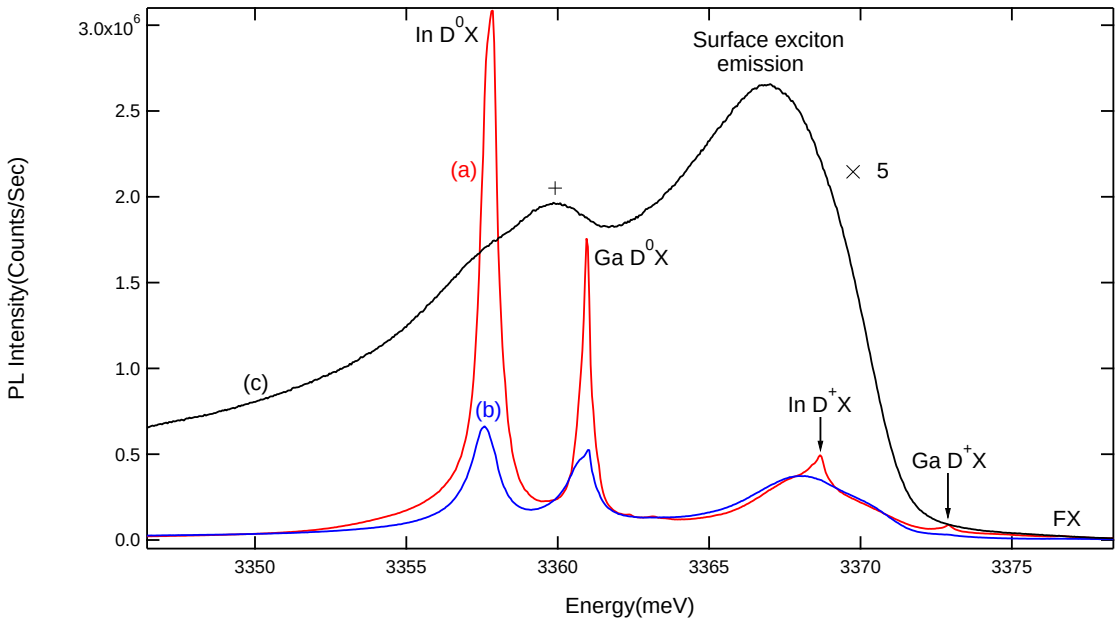

Figure 3.16: Effect of pre-growth treatment of the sapphire substrate on 4.2 K low temperature photoluminescence spectra for nominally undoped ZnO samples. (a) as received, (b) cleaned in acetone, and (c) cleaned in acetone and then annealed at 1100 °C in a tube furnace for 30 minutes with pure oxygen at a flow rate of 100 sccm. The intensity of line (c) is blown up with a factor of 5.

grown on the acetone cleaned sapphire substrate, the peak PL intensity of transitions In D^0X, and Ga D^0X becomes much weaker than that of ZnO grown on the as-received substrate, and the transitions In D^+X and Ga D^+X can not be distinguished. This may be due to the presence of surface carbon. For the epilayers grown on a cleaned and annealed sapphire substrate, two broad PL transitions are observed with linewidths 5.2 meV and 5.5 meV. The peak at 3359.86 meV labelled + is close to the Ga D^0X transition, but downshifted from the usual position by 1.1 meV. In addition there is a weaker shoulder on the low energy side which may be due to In D^0X. An additional broad peak at 3367 meV corresponds to the surface exciton energy, downshifted by 1.2 meV, in agreement with the energy shift of the Ga D^0X peak.

These data clearly show much improved strain homogeneity for the samples grown on untreated substrates, resulting in a reduction in PL linewidth by a factor of 14. One can understand the higher strain uniformity of the nanorods compared with planar films on the basis that the rods can relax laterally and should therefore have more uniform overall strain, and lower blueshift than ideal planar films, where relaxation occurs through dislocation formation. By this argument we would expect the samples grown on heat treated substrates to have both larger strain non uniformity and larger blueshift, however these samples actually show less blueshift. At this point we do not have an explanation for this reduced blueshift, but we should point out that the samples grown on heat treated substrates have complex morphology and are not ideal planar films.

3.5.2 Effect of post-growth annealing

To investigate the effect of post-growth annealing on the structural and optical properties of epitaxial ZnO thin films, nominally undoped and In-doped ZnO epilayers were annealed at 900 °C and 1000 °C under pure oxygen with a flow rate of 100 sccm for 30 minutes. The AFM measurements show that the surface morphology was greatly improved by annealing. In addition, the thickness of ZnO epilayers was found to be reduced slightly after annealing.

Figure 3.17 (a) shows a 4.2 K low temperature PL spectrum of an as-grown nominally undoped ZnO sample. Ga-related donor bound exciton transitions Ga D^0X and Ga D^+X are extremely sharp and dominant in the PL spectrum. The free exciton emission FX is also significant and sharp. The surface exciton emission is very broad and strong in the PL spec-

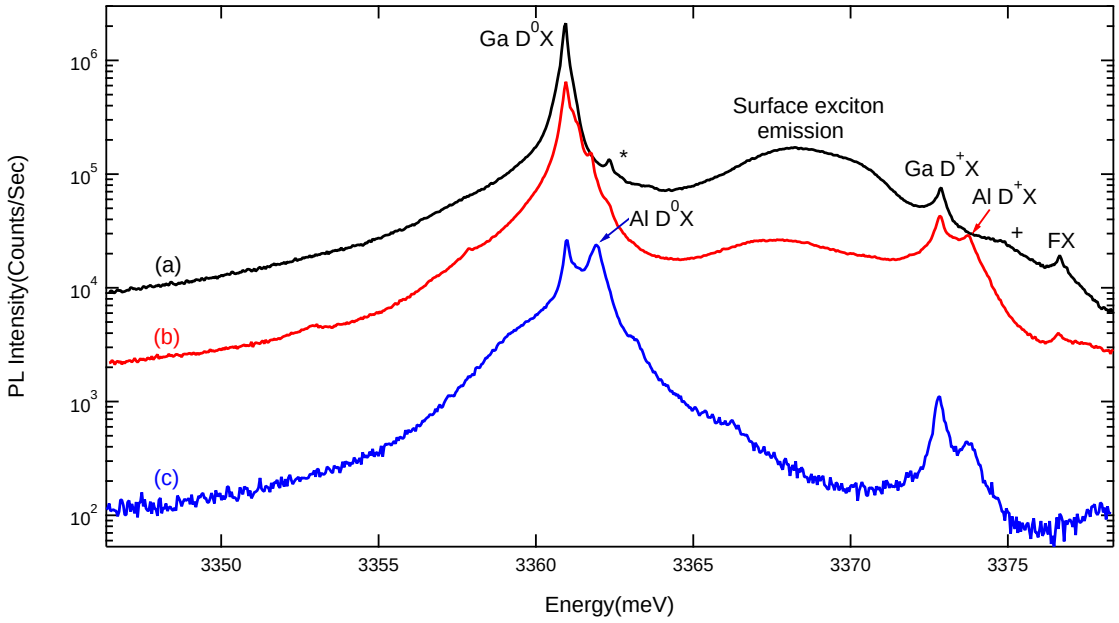

Figure 3.17: Effect of post-growth annealing on 4.2 K low temperature photoluminescence spectra of a nominally undoped ZnO sample *H*263. (a) as-grown, (b) annealed in pure oxygen ambient at 900 °C, and (c) annealed in pure oxygen ambient at 1000 °C. Data in the figure have not been offset.

trum. Figure 3.17 (b) shows the effect of annealing the same sample at 900 °C in pure oxygen for 30 minutes. There is a significant overall decrease in intensity of all bound exciton emissions after annealing. Two additional peaks located at 3361.73 meV and 3373.76 meV emerge in the spectrum after annealing at 900 °C. Considering the blueshift of 1.16 meV from the Ga-related transitions in the as-grown sample, the peak at 3361.73 meV can be ascribed to the Al-related D^0X transition. In addition, a weak peak located at 3373.76 meV is observed, which corresponds to the Al D^0X transition, due to excitons bound to ionised Al donors. The source of these Al-related features is likely out diffusion from the sapphire substrate. In addition, two transitions located at 3362.32 meV labelled with $\star$ and at 3374.76 meV labelled with $+$ disappear after annealing. These two lines do not correspond to any of the known D^0X or D^+X transitions, and may originate from a new unidentified donor impurity. Further work is required to confirm this result. Both the surface exciton emission and the free exciton emission become weaker after annealing. Increasing the annealing temperature to 1000 °C results in a steady increase in the intensity ratio of Al D^0X to Ga D^0X, which is shown in Fig. 3.17 (c). The overall intensity of the near band edge region is reduced greatly, and the surface exciton emission and free exciton emission are fully removed. The reduction in intensity may be due to the increased concentration of point defects. Room temperature Hall measurements show that the electron concentration increases significantly after annealing [31] by ~ 1 order of magnitude.

Figure 3.18 shows 4.2 K low temperature PL spectra of (a) an as-grown 1.0 sccm In-doped ZnO sample and pieces of the same sample annealed in oxygen at (b) 900 °C and (c) 1000 °C. Annealing at 900 °C in pure oxygen results in an overall intensity decrease of all the near band edge emissions. The reduction of the Ga-related transitions Ga D^0X and Ga D^+X is much faster than that of the In-related transitions In D^0X and In D^+X. A weak peak located at 3361.82 meV appears in the PL spectrum of 900 °C annealed sample, which was ascribed to the Al-related D^0X transition. In addition, a weak peak located at 3373.76 meV is observed, due to excitons bound to ionised Al donors. Increasing the annealing temperature to 1000 °C results in the complete removal of the In and Ga related D^0X and D^+X transitons. In the PL spectrum of this sample, the Al-related D^0X transition is predominant. The free exciton emission peak disappears after the thermal treatment, which again indicates that structural or point defects were introduced into the ZnO layers by annealing. Room temperature Hall measurements show a large increase in the electron

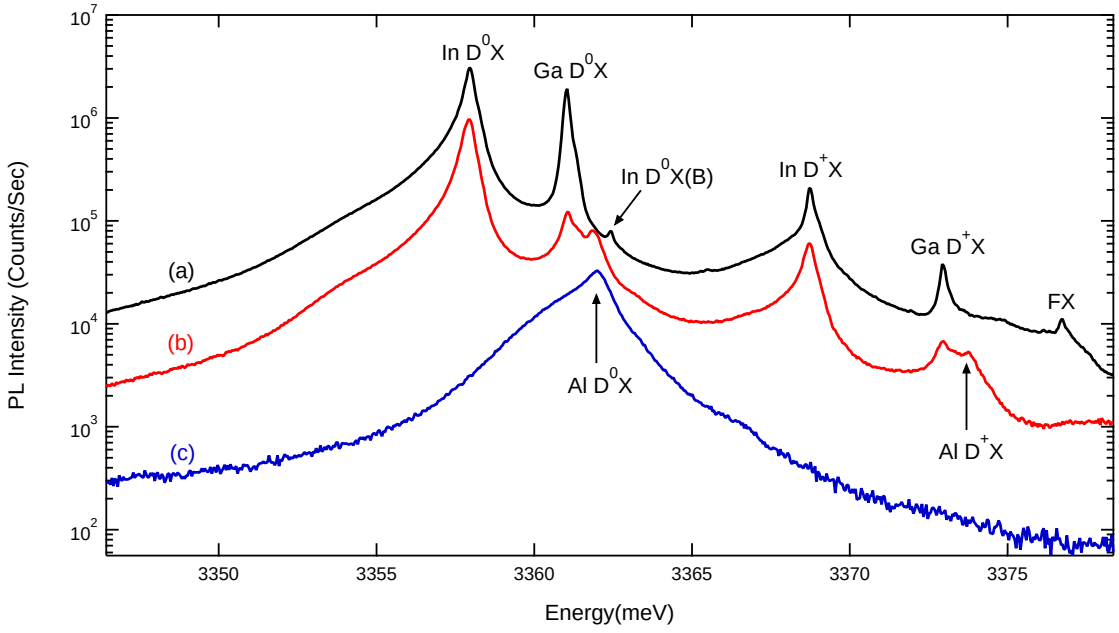

Figure 3.18: Effect of post-growth annealing on 4.2 K low temperature photoluminescence spectra of an In-doped ZnO sample *H*266 grown with 1.0 sccm TMIn flow. (a) as-grown, (b) annealed in pure oxygen ambient at 900°C, and (c) annealed in pure oxygen ambient at 1000°C. Data in the figure have not been offset. The data were published in journal of applied physics.

concentration after annealing [31], which is consistent with the increase of point defects.

3.5.3 Conclusions

Pre-growth sapphire substrate annealing results in an improvement in epilayer morphology by promoting more lateral growth. However, this appears to result in a large broadening in the bound exciton transitons. The most likely origin is increased non-uniform strain. Post-growth annealing under oxygen above the growth temperature causes out-diffusion of Al from the sapphire substrate into the ZnO layers. The reduction and removal of the Ga and In related donor bound exciton transitions after post-growth annealing imply a high diffusivity of these substitutional donors in our ZnO thin films.

Chapter 4

Raman results

Raman scattering spectroscopy is one of the main techniques used in this work, due to its high sensitivity for thin layers and nondestructive nature. It is an effective tool to study lattice dynamics and electronic properties. Raman scattering spectroscopy is commonly used to obtain information on zone-center and some zone-boundary phonon modes in single crystal semiconductors. In addition, Raman scattering spectroscopy is sensitive to vibrational modes of impurities and defects through the observation of local vibrational modes (LVMs) which are localized in both real space and frequency space.

4.1 Introduction

A lattice phonon is a quantized vibrational mode of the crystal lattice. In a material with at least two atoms per unit cell such as ZnO, the different atoms can vibrate either in phase or out of phase, which respectively gives rise to optical and acoustic phonon modes. A normal mode vibrating parallel to the propagation direction of the wave is called a longitudinal phonon mode; a normal mode vibrating perpendicular to the direction in which the wave propagates is called a transverse phonon mode. In general, the total number of normal vibrational modes for a crystal with s atoms per unit cell is $3s$. For cubic materials, 3 of them are acoustic phonon modes and the remaining $3s-3$ normal vibrational modes are optical phonon modes. For single crystal ZnO having the wurtzite structure, the number of atoms in the unit cell is $s=4$. According to factor group analysis, at the center of the Brillouin zone there are twelve normal vibrational modes: namely, one longitudinal

acoustic phonon (LA), two transverse acoustic phonons (TA), three longitudinal optical phonons (LO) and six transverse optical phonons (TO) [55].

4.1.1 Theory of Raman scattering

Raman scattering involves inelastic light scattering by a crystal lattice or molecule. By interacting with the elementary excitations of a crystal lattice such as phonons, plasmons, and coupled phonon-plasmons, the incident photon will lose or gain energy to produce a scattered photon. When light with frequency ω_i is incident on a semiconductor surface, part of the incident light is transmitted or absorbed; but in addition, scattering of the laser light by phonons can also occur. The scattered radiation contains not only the frequency ω_i associated with the incident light, called Rayleigh scattering; but also a pair of new frequencies $\omega_i \pm \omega_q$ corresponding to absorption or emission of a phonon, called Raman scattering. The frequency of the elementary lattice excitation involved in a scattering process can be determined from the Raman spectrum using the law of conservation of energy:

$$\hbar\omega_s = \hbar\omega_i \pm \hbar\omega_q \tag{4.1}$$

where $\hbar\omega_s$ is the energy of the scattered photon and $\hbar\omega_q$ is the energy of the elementary lattice excitation. The minus sign refers to Stokes scattering, in which the crystal absorbs energy and an elementary lattice excitation is generated. The plus sign refers to anti-Stokes scattering, in which the crystal loses energy and results in the annihilation of an elementary lattice excitation.

The quantum mechanical picture of Raman light scattering can be described as follows (here we just consider the first order Raman scattering) [56]. First, the incident photon influences and distorts the electron cloud in the crystal lattice which results in the creation of a virtual state. At the same time, an electron is excited from the ground state to this virtual state to create an electron-hole pair due to the annihilation of the incident photon. The virtual state has a very short life time. From this point, things will occur in different ways for different kinds of scattering. In Rayleigh scattering, the electron-hole pair does not interact with the phonon of the lattice and therefore there is no energy transfer. Thus, in Rayleigh scattering the electron will quickly jump back to the ground state from the virtual state and emit a photon with the same frequency as the incident light as shown in

Fig. 4.1 (a). In Stokes scattering, the electron-hole pair interacts with the lattice and creates a lattice phonon or local vibrational mode of an impurity atom by losing some energy. Therefore, after recombination of the electron-hole pair the scattered photon will have a lower frequency than the incident one as shown in Fig. 4.1 (b). In anti-Stokes scattering, the electron-hole pair interacts with the lattice and gains some energy by annihilating a phonon. Hence, after recombination of the electron-hole pair the scattered photon will have a higher frequency than the incident one as shown in Fig. 4.1 (c).

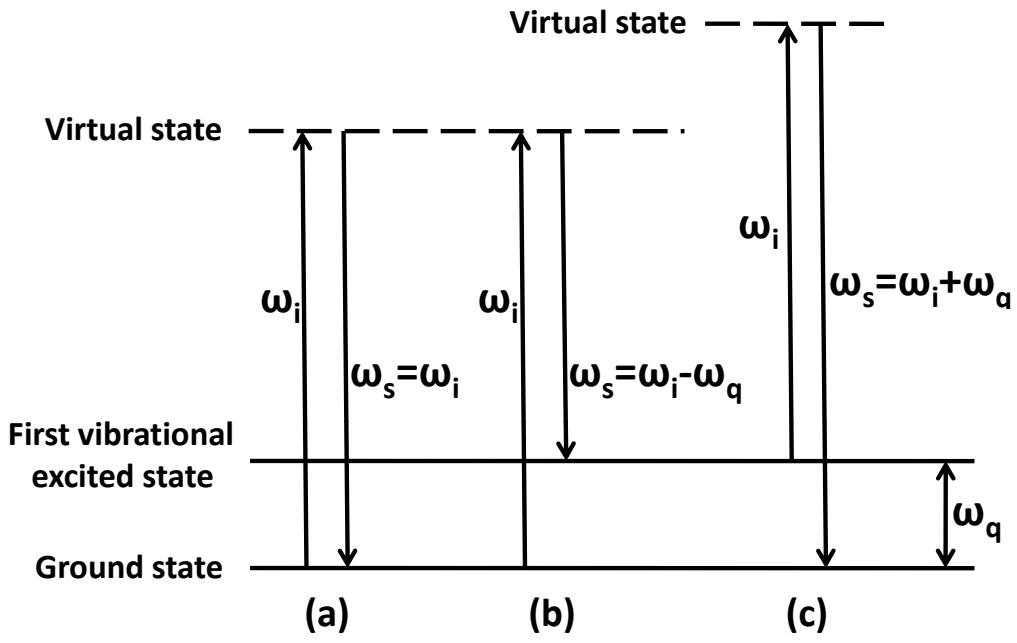

Figure 4.1: Schematic description of (a) Rayleigh scattering, (b) Stokes scattering and (c) anti-Stokes scattering.

4.1.2 Selection rules

In classical theory, we consider the incident light as an electromagnetic field described by:

$$E = E_0 cos(\omega_i t) \tag{4.2}$$

where E and ω_i are the electric field vector and frequency of the incident light. An electric dipole moment p is induced by the incoming laser light:

$$p = \alpha \cdot E \tag{4.3}$$

where α is the polarizability tensor of the crystal. We assume that the crystal vibrates as a simple harmonic oscillator. A particular mode is vibrating with a frequency ω_q, so the atom displacement q is given by:

$$q = q_0 cos(\omega_q t) \tag{4.4}$$

The polarizability tensor α can be Taylor expanded with respect to the normal-mode coordinate q_k:

$$\alpha_{mn} = (\alpha_{mn})_0 + \sum_k (\frac{\partial \alpha_{mn}}{\partial q_k})_0 q_k + \ldots \tag{4.5}$$

where the subscript 0 represents the value at the equilibrium position. The polarizability tensor of the crystal is given by a matrix ($[\alpha_{mn}]$). In the harmonic approximation, we just consider the first two terms in the right hand side of Eqn. 4.5. Therefore, the electric dipole moment p can be rewritten:

$$\begin{aligned} p &= \alpha \cdot E \\ &= \alpha_0 E_0 cos(\omega_i t) + \sum_k (\frac{\partial \alpha}{\partial q_k})_0 (q_k)_0 cos(\omega_q t) E_0 cos(\omega_i t) \\ &= \alpha_0 E_0 cos(\omega_i t) + \frac{1}{2} \sum_k (\frac{\partial \alpha}{\partial q_k})_0 (q_k)_0 E_0 [cos(\omega_i + \omega_q)t + cos(\omega_i - \omega_q)t] \end{aligned} \tag{4.6}$$

Equation 4.6 shows that the induced electric dipole moment has three different frequencies ω_i, $\omega_i + \omega_q$ and $\omega_i - \omega_q$, which correspond to Rayleigh scattering, Stokes scattering and anti-Stokes scattering, respectively. Therefore, the condition for Raman activity is that at least one of the components of the polarizability tensor must have a nonzero derivative with respect to the normal mode coordinate at the equilibrium position.

According to the law of conservation of crystal momentum, we can get the wavevector of a phonon from:

$$k_s = k_i \pm q \tag{4.7}$$

where k_i, k_s and q represent the wavevectors of the incident photon, the scattered photon and the lattice phonon, respectively. The magnitude of the wavevector of the scattered light is dependent on the geometry of the Raman system. In this thesis, we use a backscattering micro-Raman facility. Hence, the magnitude of q is equal to the sum of the magnitude of k_i and k_s. For the visible laser we used in this work, the magnitude of k_i is around 10^5 cm^{-1} which is three orders of magnitude smaller than the wavevectors corresponding to the Brillouin zone boundaries in semiconductor ZnO. Under these conditions, Raman scattering is only active for phonons near the Brillouin zone center (i.e. $q \sim 0$).

4.1.3 Local vibrational modes

Impurities such as hydrogen and carbon are omnipresent in the metalorganic vapour phase epitaxy (MOVPE) environment. The incorporation of H or C into the ZnO crystal may result in a significant change in the electronic and vibrational properties of semiconductoring ZnO. Impurity atoms less massive than the host atoms always show some new vibrational modes, called local vibrational modes (LVMs). Unlike the lattice phonons we discussed previously, the vibrational modes of the defects are localized to the impurity atom and its nearest neighbors. In addition, the LVM is also restricted in frequency space giving rise to sharp peaks in the Raman scattering spectrum. Generally LVMs occur above the allowed phonon energies of lattice modes (except for gap modes).

To make things simple, we assume that the vibrational mode of the defect is completely localized on the impurity atom itself. The oscillation of the impurity atom can be described by:

$$m_{imp}\ddot{x} + kx = 0 \tag{4.8}$$

where m_{imp} is the mass of the impurity atom, which is less massive than the host atom. x is the displacement of the impurity atom and k is the force constant between the impurity atom and the nearest neighbors. The solution of Eqn. 4.8 is given by:

$$x = x_0 e^{i\omega_{LVM}t} \tag{4.9}$$

$$\omega_{LVM} = \sqrt{\frac{k}{m_{imp}}} \tag{4.10}$$

where ω_{LVM} is the vibrational frequency of the impurity atom. Equation 4.10 tells us that the local vibrational frequency is highly dependent on the mass of the impurity atom. The lighter the mass of the impurity atom, the higher the frequency of the impurity mode. If we take into account the nearest neighbors around the impurity atom, the angular frequency can be given by [57]:

$$\omega_{LVM} = \sqrt{k(\frac{1}{\chi M} + \frac{1}{m_{imp}})} \tag{4.11}$$

where M is the mass of the nearest neighbor, and χ is an empirical constant which is dependent on the local bond.

Because of the Raman selection rules, only six optical phonons $A_1(TO)$, $A_1(LO)$, $E_1(TO)$, $E_1(LO)$, $E_2(high)$ and $E_2(low)$ are active in the first-order Raman scattering of semiconductoring ZnO [29]. The A_1 and E_1 symbols here label the symmetries in which the atoms vibrate in a direction parallel or perpendicular to the c-axis of the ZnO, respectively. The $E_2(low)$ mode is associated with vibrations of the Zn sublattice, while the $E_2(high)$ mode involves only the O sublattice. In the case of backscattering geometry, the incident light is perpendicular to the surface (i.e. parellel to the c axis). In this case, only $E_2(high)$, $E_2(low)$ and $A_1(LO)$ modes are expected to be observed in unpolarized Raman spectra, and the other first-order Raman scattering modes are forbidden according to the selection rules.

4.2 Effect of growth temperature on the electronic and vibrational properties of ZnO

4.2.1 Effect of growth temperature

The growth temperature is a key factor that influences the rate and mechanism of the chemical reactions in the deposition process, which should lead to changes in the crystal quality, and therefore in the intensity and position of lattice phonons and local vibrational modes. To investigate the effect of growth temperature on the lattice structure and chemical content of the layers, a series of ZnO samples were grown on c-plane sapphire substrates by

MOCVD. Diethylzinc (DEZn, $(C_2H_5)_2Zn$) and nitrous oxide (N_2O) were used as the Zn and O precursors with flow rates of 40.0 sccm and 1.0 slm, respectively. For each sample, the growth time was 30 minutes. Raman spectra of samples fabricated at different growth temperatures are shown in Fig. 4.2. The 457.9 nm line of an argon ion laser was used as the excitation source.

In Fig. 4.2, the Raman feature located at 435.8 cm^{-1} is assigned to the high frequency E_2 mode of the ZnO crystal [29, 58, 59]. It becomes sharper and stronger with increasing growth temperature and reaches a maximum at 600 °C, after which it decreases with increasing growth temperature. The peak at 331.1 cm^{-1} is the second order Raman signal arising from zone-boundary (M point) phonons ($2E_2(M)$) of the ZnO crystal [29, 58, 60] (point M is the center of a specific side face of the Brillouin zone). The intensity of this peak changes in the same way as the $E_2(H)$ transition with the change of the growth temperature. The peak at 1156 cm^{-1} is assigned to the second order $E_1(LO)$ mode of the ZnO crystal [61]. This $2E_1(LO)$ peak first appears at 550 °C and rises to a maximum at 600 °C, followed by a decrease in intensity as the growth temperature increased further. Two additional peaks at 507 cm^{-1} and 1983 cm^{-1} are only observed in the spectra of samples grown at low temperatures. The intensity of these two peaks decreases as the growth temperature is increased, and completely vanish at 550 °C. Some previous papers interpret these modes as local vibrational modes due to hydrogen complexes [61]. This seems like a suitable explanation based on the fact that hydrogen atoms are much more mobile at high temperatures [43]. The source of the hydrogen is probably the DEZn precursor. There is an additional peak located at 274 cm^{-1}, which is only observed in the spectrum of the 600 °C ZnO. Some researchers suggested that this transition was related to nitrogen doping resulting from the O precursor N_2O [62]. Peaks located at 379.2, 416.2, 575.9 and 747.7 cm^{-1} belong to Raman features of the sapphire substrate, which is proven by the Raman spectrum of a sapphire substrate shown in Fig. 4.3. Although the $A_1(LO)$ mode of ZnO is expected to appear at 574 cm^{-1}, there is no way to distinguish it from the sapphire Raman peaks. The appearance of Raman signals of the substrate in Fig. 4.2 indicates that the penetration depth of this 457.9 nm laser line is more than 0.5 μm for the epitaxial ZnO thin film (the average thickness of ZnO thin films for the samples in Fig. 4.2 is about 0.5 μm). This is expected since the laser energy of 2.71 eV is below the 3.37 eV bandgap of ZnO.

As shown in Fig. 4.2, Raman spectra of low temperature samples show two broad peaks

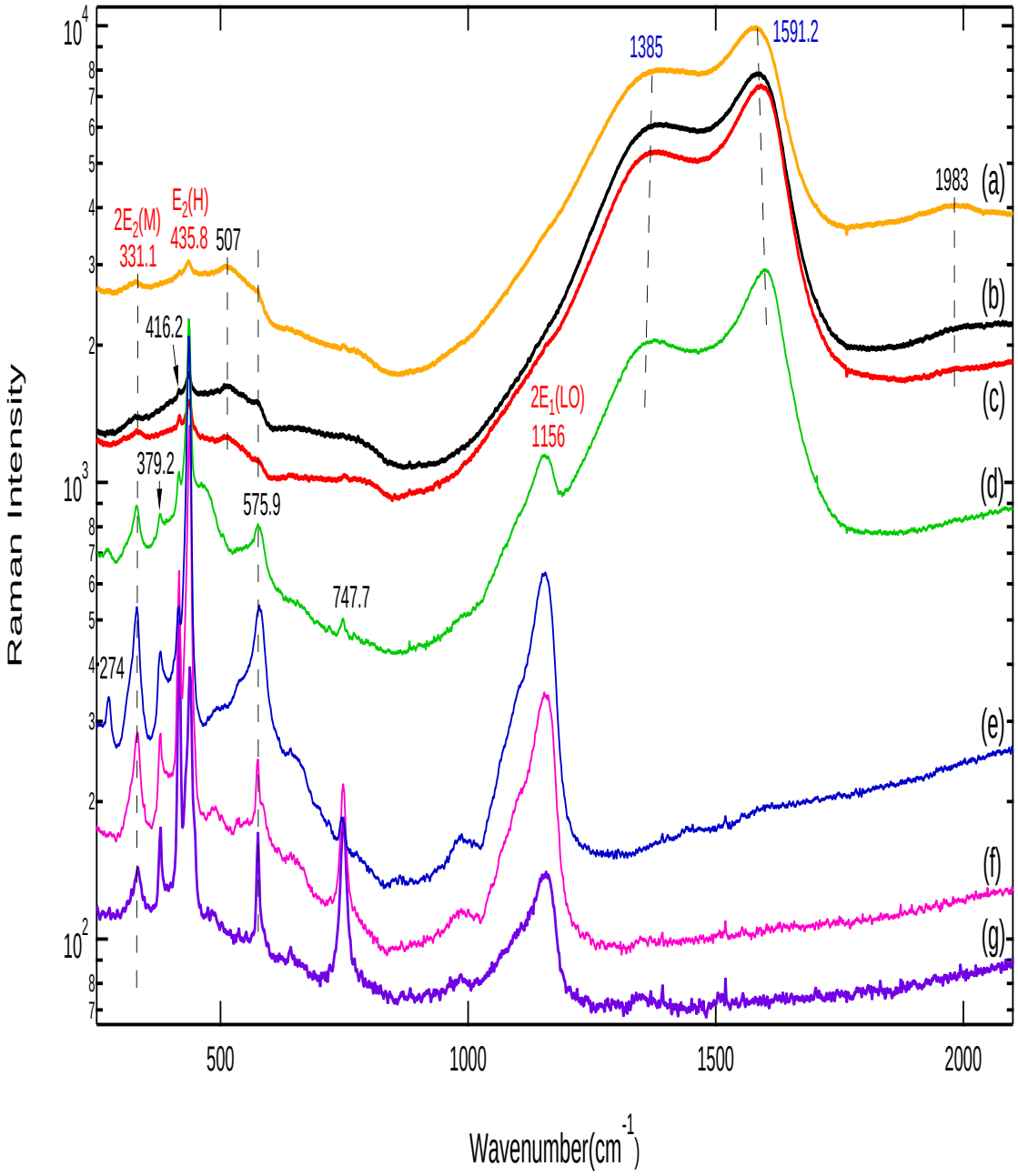

Figure 4.2: Raman backscattering spectra of samples grown at (a) 350 °C, (b) 400 °C, (c) 450 °C, (d) 550 °C, (e) 600 °C, (f) 700 °C and (g) 800 °C. Data in the figure have not been offset.

at around 1350 cm^{-1} and 1600 cm^{-1} which agree with the D and G lattice phonon modes of graphite, which indicates that a large concentration of carbon atoms is incorporated into ZnO layers forming sp^2 carbon. The D peak is interpreted as a breathing mode of A_{1g} symmetry arising from phonons near the K zone boundary (point K is the middle of an edge joining two side faces). The D phonon mode is normally forbidden in bulk graphite, but becomes increasingly allowed for smaller nanoparticles. The G peak is assigned to a mode with E_{2g} symmetry involving the in-plane bond-stretching motion of pairs of carbon sp^2 atoms. The integrated intensity ratio of the D peak to the G peak is given by the following expression [63]:

$$\frac{I(D)}{I(G)} = C(\lambda)L_a^2 \tag{4.12}$$

where $C(\lambda) \sim 0.0055\ \mathring{A}^{-2}$ at $\lambda = 515.5\ nm$, and L_a is the average cluster size of carbon sp^2 clusters. For the samples in Fig. 4.2, the intensity of D and G modes are obtained by Gaussian fit. The integrated intensity ratios $\frac{I(D)}{I(G)}$ are equal to 0.81, 0.78, 0.72 and 0.70, corresponding to growth temperatures at 350 °C, 400 °C, 450 °C and 550 °C, respectively. The cluster sizes are estimated to be 12.1 Å, 11.9 Å, 11.4 Å and 11.3 Å. This indicates that

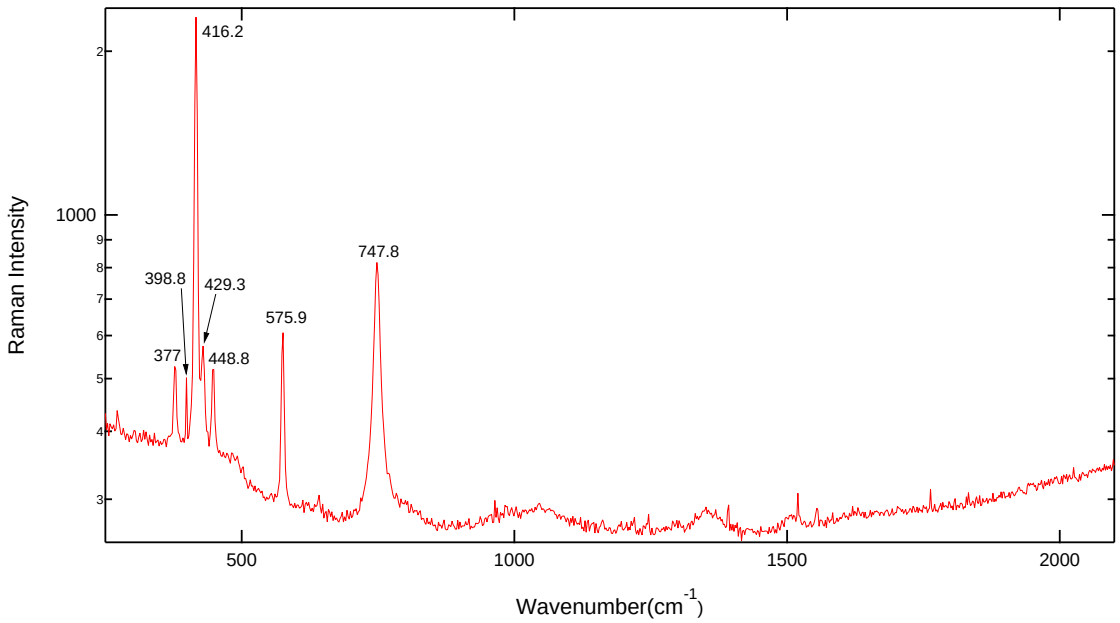

Figure 4.3: Raman backscattering spectrum of sapphire substrate.

the size of carbon cluster does not change significantly with increasing growth temperature. The length of the sp^2 $C-C$ bond is 2.461 Å. This implies that the carbon clusters in ZnO layers involve a very small number of C atoms. The reduction in the peak intensity of the D and G modes suggests that the density of carbon clusters decreases with increasing growth temperature. For the samples grown above 550 °C, the D and G modes are strongly suppressed. At 800 °C, they are not detected. Nickel et al. reported a cluster size of 21 Å for undoped ZnO and 27.6 Å for N-doped ZnO [61] based on similar analysis. Tang et al. reported a cluster size of 16.4 Å for undoped ZnO and 33.8 Å for N-doped ZnO [62]. Chen et al. reported cluster sizes of N-doped ZnO ranging from 15.1 Å to 21.1 Å [59].

In summary, the Raman spectra in Fig. 4.2 show that the ZnO lattice phonon modes are enchanced while the graphite modes are suppressed with increasing growth temperature. It is likely that the suppression of carbon is due to the high temperature reaction between the hydrocarbon radicals and the nitrous oxide source. The increased intensity of the lattice modes with temperature shows an improvement in the crystal quality of the ZnO thin films above 550 °C.

4.2.2 Distribution of carbon clusters

To investigate the distribution of carbon clusters in the ZnO epilayers, etching experiments were carried out on ZnO grown on (111) silicon substrates. This ZnO sample was grown with DEZn and N_2O with flow rates of 80.0 sccm and 2.0 slm, respectively. The growth temperature was 450 °C. Figure 4.4 shows a schematic cross-section of the ZnO sample after etching in NH_4Cl(aq). A step was formed by partially covering the surface of ZnO layers with crystal bond wax, then etching with 5% NH_4Cl(aq). This procedure was repeated several times to create a series of steps as shown in Fig. 4.4. The step heights were measured by Dichen Li using a surface profilometer. During the measurement, we found that the etched surfaces are pretty rough. From left to right, the heights of steps range from 10.3 nm to 355.5 nm, from 1.9 nm to 13.3 nm, and from 69.2 nm to 92.3 nm.

Figure 4.5 shows Raman scattering spectra of the step-by-step etched ZnO sample shown in Fig. 4.4 with the incident laser line focussed on different steps. The silicon longitudinal optical mode located at 520.07 cm^{-1} is dominant in the spectrum. The ZnO $E_2(H)$ mode at 437.9 cm^{-1} is weak compared with the silicon peak, and its intensity is reduced

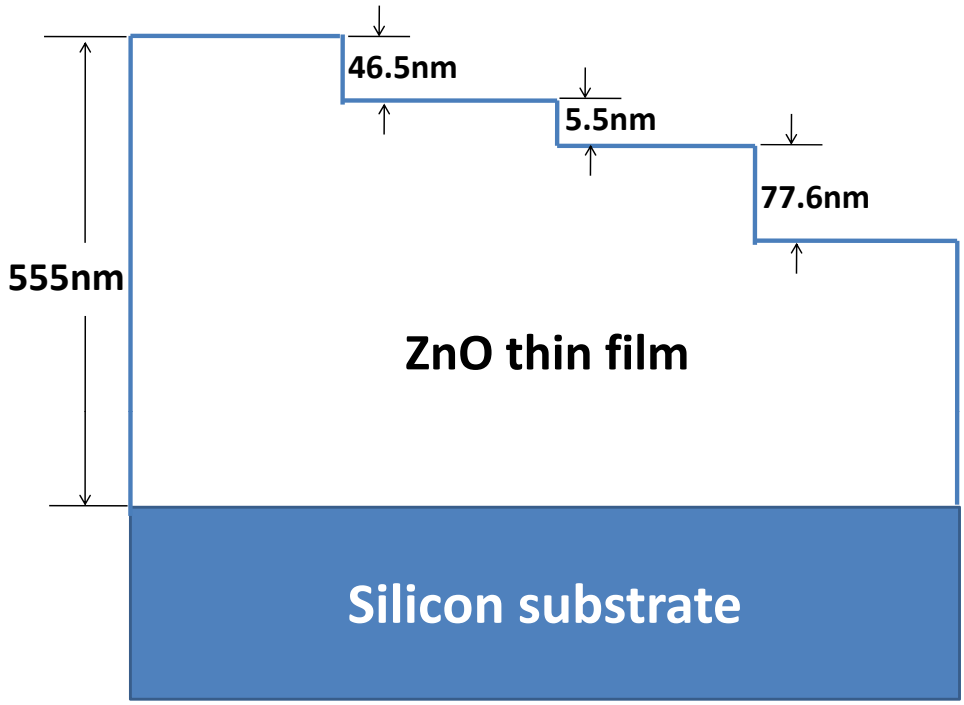

Figure 4.4: A schematic graph of the ZnO sample after etching in NH_4Cl(aq). The etching thickness was measured with a profilometer in 4D LABS by Dichen Li.

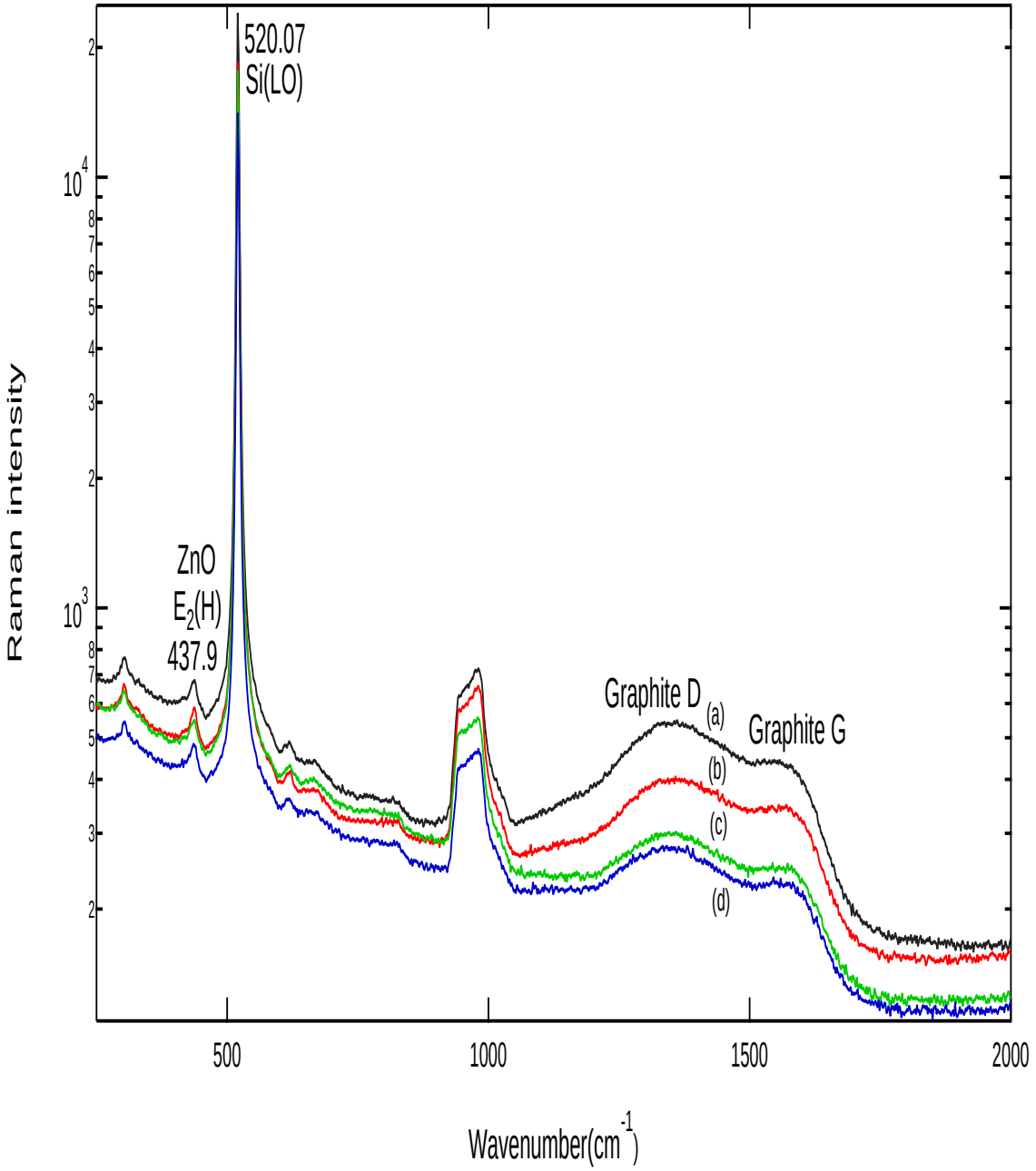

Figure 4.5: Raman backscattering spectra of ZnO sample etching by NH_4Cl(aq). The incident laser was focused on the region with (a) no etching, (b) etching away 46.5 nm, (c) etching away 52.0 nm and (d) etching away 129.6 nm. Data in the figure have not been offset.

by etching. The graphite lattice phonon modes D and G are observed in all of the Raman spectra and decreased in intensity as the etching depth increased. This strongly indicates that the carbon clusters are distributed throughout in the thin films and not just at the surface. The integrated intensity ratios $\frac{I(D)}{I(G)}$ are 1.22, 1.16, 1.18 and 1.21, corresponding to the highest to lowest steps in Fig. 4.4, respectively. These values are pretty close to each other, which shows that the size of the carbon clusters does not change with etching. However, the intensity of D and G modes decreases with etching, which implies a reduction of the integrated number of carbon clusters.

4.3 Effect of annealing on the electronic and vibrational properties of the epitaxial ZnO thin film

The effect of post-growth annealing on the structural properties of ZnO samples can also be revealed by Raman scattering spectroscopy. The annealing temperature and annealing ambient are two important factors in the thermal annealing process. The annealing temperature ranges from 600 °C to 800 °C. The annealing ambient was either pure nitrogen or pure N_2O. For samples grown at low temperature, peaks related to lattice phonon modes of graphite are always observed in the Raman spectrum. It is of interest to investigate whether the carbon observed in Raman measurements can be removed by thermal annealing.

4.3.1 Effect of annealing temperature

To investigate the effect of the annealing temperature on the lattice structure and vibrational modes, a series of ZnO samples were grown on *c*-plane sapphire substrates by MOCVD. DEZn and N_2O were used as the Zn and O precursors with flow rates of 40.0 sccm and 1.0 slm, respectively. The layers were grown at 500 °C for 30 minutes. After growth, samples $H045$, $H046$ and $H047$ were annealed in the reactor with 1.0 slm N_2O flow for 30 minutes. There was no post-growth annealing for sample $H044$. The annealing information of these samples is shown in Table 4.1.

Figure 4.6 (a) shows a Raman spectrum of an as-grown ZnO sample grown at 500 °C, which is in good agreement with the Raman features of previous low growth temperature samples. The ZnO lattice phonon modes $E_2(H)$ and $2E_{2M}$ are very weak, while the graphite

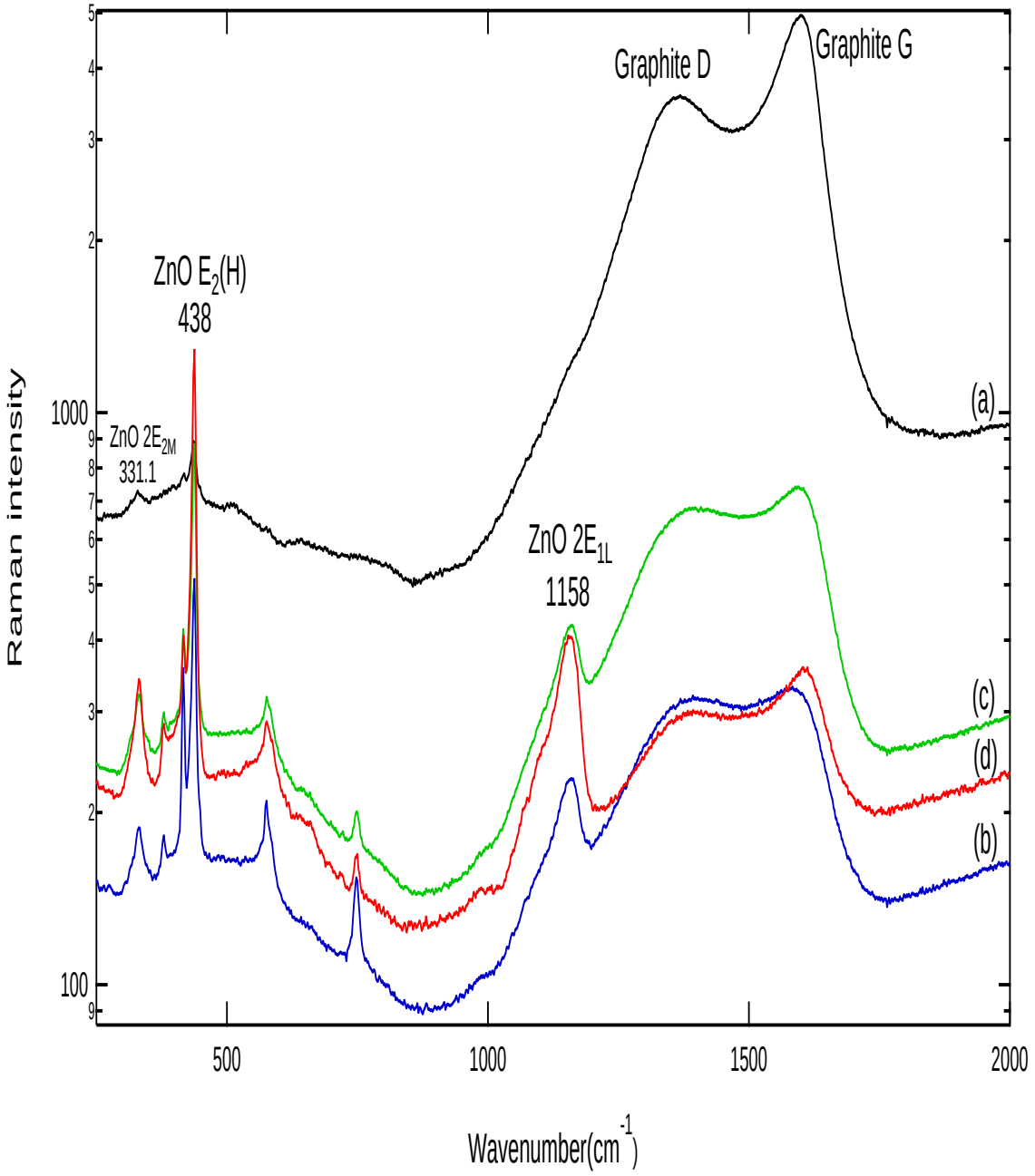

Figure 4.6: Raman scattering spectra of ZnO samples post-growth annealed at (a) no annealing, (b) 600 °C, (c) 700 °C and (d) 800 °C, with 1.0 slm N_2O flow. Data in the figure have not been offset.

Table 4.1: Annealing temperature and layer thickness of samples $H044$, $H045$, $H046$ and $H047$.

Sample Number	Annealing temperature $^{\circ}C$	Thickness (nm)
$H044$	no annealing	565
$H045$	600	542
$H046$	700	554
$H047$	800	582

lattice phonon modes D and G are very strong. Figure 4.6 (c) and (d) show Raman spectra of ZnO epilayers which were post-growth annealed at 700 °C and 800 °C in 1.0 slm N_2O, respectively. The intensity of the ZnO lattice phonon modes became stronger while the graphite D and G phonon modes became weaker as the annealing temperature was increased. For the sample post-growth annealed at 600 °C, the Raman spectrum is shown in Fig. 4.6 (b) with a huge decrease in the intensity of graphite phonon modes. However, the intensity of the ZnO lattice phonon modes such as $E_2(H)$, $2E_{1L}$ and $2E_{2M}$ is still low without an expected increase. The intensity ratios $\frac{I(D)}{I(G)}$ were found to be 0.724, 0.966, 0.918 and 0.844 for the as-grown, 600 °C, 700 °C, and 800 °C post-growth annealed samples, respectively. According to Eqn. 4.12, the corresponding carbon cluster size is equal to 11.5 Å, 13.2 Å, 12.9 Å and 12.4 Å again indicating no appreciable change in nano particle size. However, the strong reduction in D and G intensity does indicate a big reduction in the carbon nano particle concentration. A higher annealing temperature such as 700 °C and 800 °C should accelerate the chemical reaction between the carbon atoms and the N_2O oxygen precursor, resulting in the remove of carbon from the ZnO thin films. Therefore, samples annealed at 700 °C and 800 °C show much weaker graphite modes as well as enhanced ZnO Raman modes due to increased crystallinity of the ZnO epilayer.

4.3.2 Effect of annealing ambient

It is interesting to determine the effect of the gas ambient on the annealing behavior of the low temperature grown ZnO samples. Sample $H065$ was grown with DEZn and N_2O as

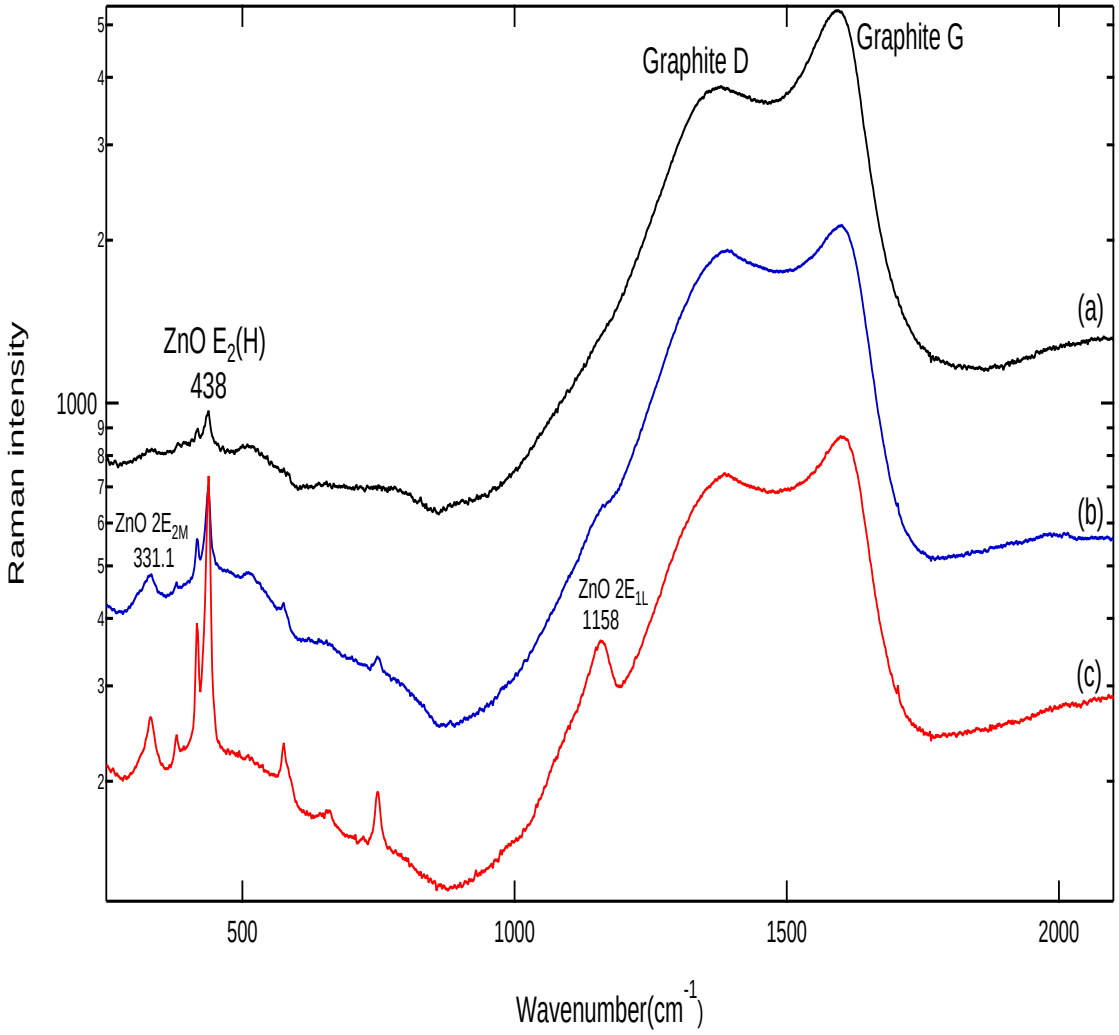

Figure 4.7: Raman scattering spectra of ZnO samples post-growth annealed in (a) no annealing, (b) N_2 at 800 °C, and (c) N_2O at 800 °C. Data in the figure have not been offset.

the Zn and O precursors with flow rates of 40.0 sccm and 2.0 slm, respectively, at 450 °C on a *c*-plane sapphire substrate. The growth time was 30 minutes resulting in a ZnO film with a thickness of 550 nm. To investigate the effect of annealing ambient on the carbon impurities, three pieces of sample *H*065 were treated in different ways. The first piece was untreated as a reference; the second one was annealed in pure N_2 gas at 800 °C for 30 minutes; and the third one was annealed in pure N_2O gas at 800 °C for 30 minutes. Raman measurements were taken separately on these three pieces of *H*065.

Figure 4.7 (a) shows a Raman spectrum of the as-grown sample *H*065. The graphite D and G phonon modes have quite strong intensity, while just one phonon mode of the ZnO lattice $E_2(H)$ appears at 438 cm^{-1} and its intensity is very low compared with the graphite peaks. Figures 4.7 (b) and (c) show Raman spectra of samples *H*065, which went through post-growth annealing in N_2 and N_2O, respectively. The larger reduction in intensity of the graphite D and G modes for the sample annealed in N_2O than the sample annealed in N_2 is consistent with a reaction between carbon atoms and N_2O. In addition, annealing in both ambients leads to an improvement in the crystal quality, shown by the fact that the ZnO lattice phonon modes became stronger.

4.4 Effect of intentional carbon doping

As discussed previously, impurity atoms and point defects which are less massive than the host atoms could introduce additional local vibrational modes. The incorporation of carbon atoms is unavoidable in ZnO thin films grown by MOCVD. However, as we showed previously, at low growth temperatures the unintentionally doped carbon atoms prefer to form sp^2 carbon clusters, which produce graphite lattice phonon modes D and G. Intentional carbon doping with the precursor CCl_4 was undertaken in an attempt to introduce carbon point defects such as carbon substituted on oxygen sites (C_O).

In this section, a series of intentionally C-doped ZnO samples were grown by MOCVD on *c*-plane sapphire substrates in order to search for spectroscopic evidence of isolated carbon atom point defects. Such defects are of great technological importance in III-V semiconductors such as GaAs, where they usually cause p-type doping. For these samples, a two-step deposition method was used. DEZn and N_2O were used as the Zn and O precursors with flow rates of 40.0 sccm and 2.0 slm, respectively. A thin buffer layer was

Table 4.2: Flow rates of carbon dopant CCl_4 when fabricating samples $H091$, $H092$, $H093$, $H094$, $H095$ and $H096$.

Sample Number	Flow rate of CCl_4 (sccm)
$H092$	0
$H094$	2
$H093$	5
$H095$	10
$H096$	20
$H091$	100

first grown at 500 °C for 5 minutes, and then ZnO thin film deposition occurred at 800 °C for 40 minutes. The purpose of the buffer layer was to improve the surface roughness of the high temperature layer. For 800 °C growth, a C precursor (CCl_4) was introduced into the reactor with different flow rates to form the samples listed in Table 4.2. Sample $H092$ grown without CCl_4 doping has a film thickness of 306 nm, which is used as a reference. The intentionally C-doped ZnO samples have a dull and rough surface, which makes it impossible to measure its thickness using optical reflectance measurements. However, the strength of the ZnO lattice peaks relative to those of sapphire indicate appreciable film thickness.

Figure 4.8 shows the effect of increasing CCl_4 concentration on the Raman spectra. The expanded version of the region from 250 cm^{-1} to 500 cm^{-1} is shown in Fig. 4.9. The intensity of the ZnO lattice phonon modes such as $E_2(H)$, $2E_{1L}$ and $2E_{2M}$ increases steadily with increasing CCl_4 flow rate, which implies that intentional carbon doping leads to an improvement in the lattice structure of the ZnO epilayers. As we discussed previously, the ZnO lattice phonon mode $A_1(LO)$ overlaps with the Raman feature of sapphire substrate at 575.9 cm^{-1}. But the $A_1(LO)$ mode is separated from the sapphire phonon mode in the Raman spectra of intentionally C-doped ZnO samples. One piece of evidence to support this assignment is that the peak located at 580.2 cm^{-1} shows an intensity increase similar to the phonon modes $E_2(H)$, $2E_{1L}$ and $2E_{2M}$. An additional peak at 276.1 cm^{-1} emerges in the Raman spectra of intentional C-doped ZnO samples, and its intensity increases steadily

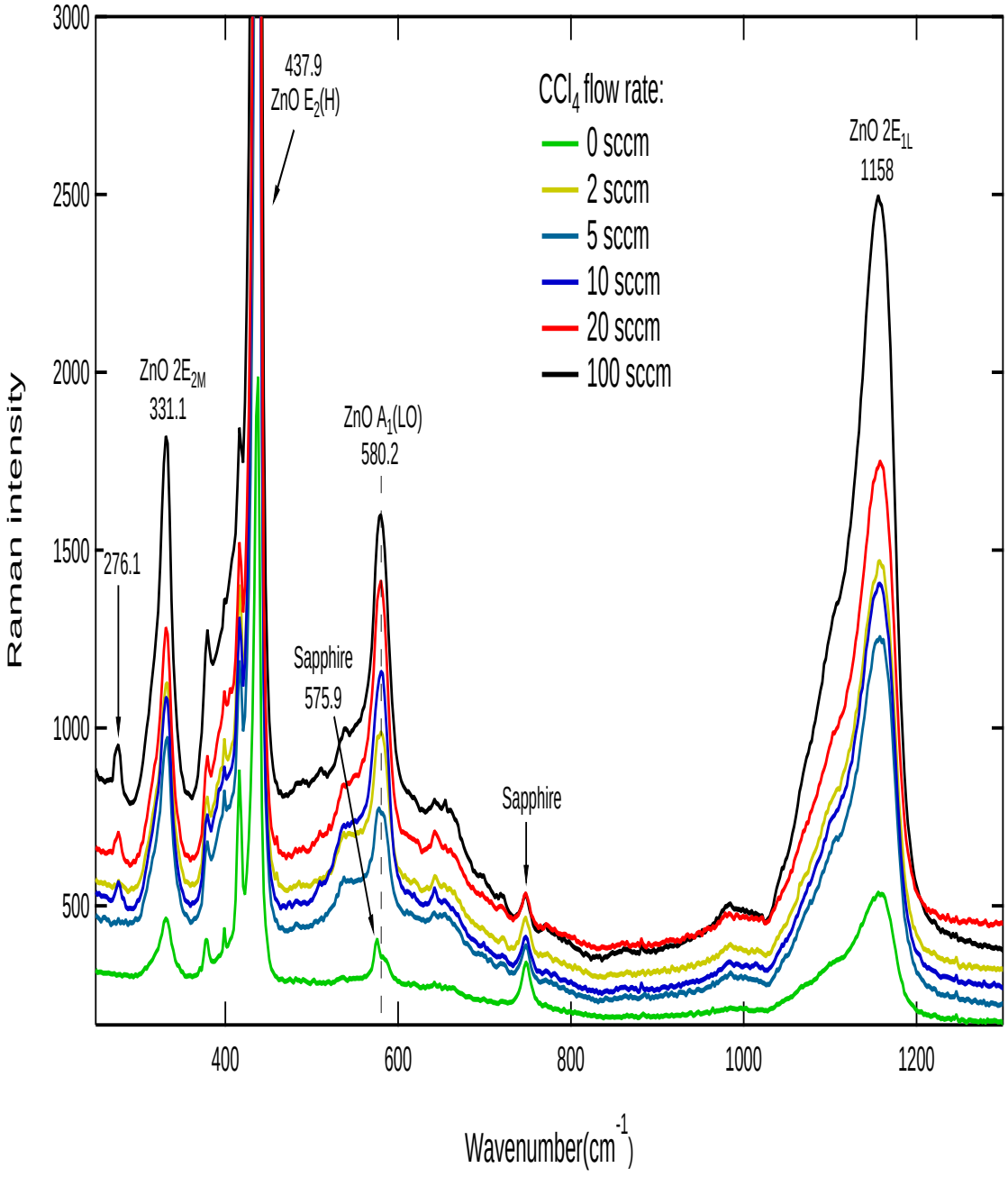

Figure 4.8: Raman scattering spectra of intentionally C-doped ZnO samples. The carbon precursor CCl_4 flow rate ranges from 0 *sccm* to 100 *sccm*.

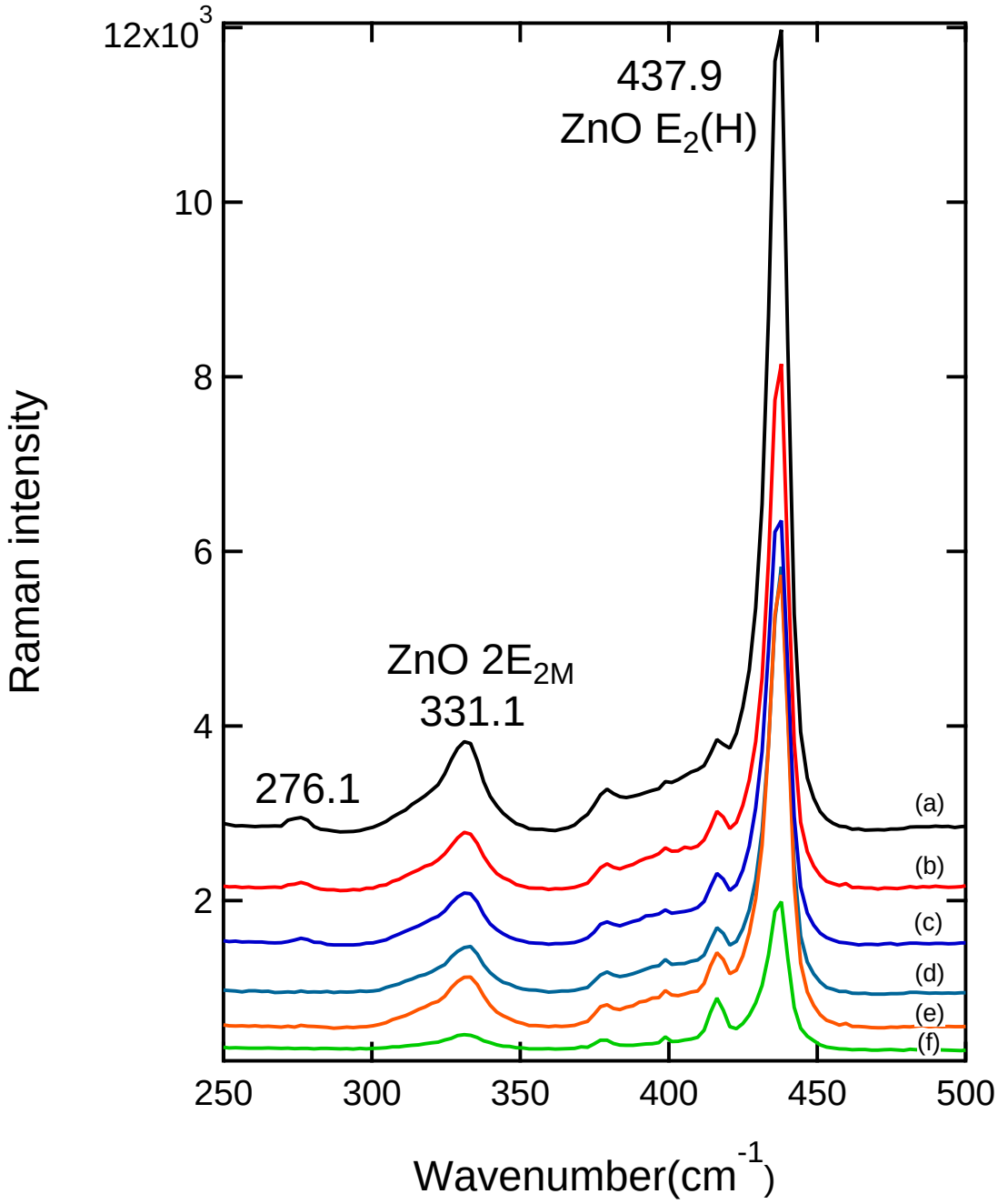

Figure 4.9: Raman scattering spectra of intentionally C-doped ZnO samples. The carbon precursor CCl_4 flow ranges were (a) 100 *sccm*, (b) 20 *sccm*, (c) 10 *sccm*, (d) 5 *sccm*, (e) 2 *sccm* and (f) 0 *sccm*. The following *y* axis offsets were applied to the data: (a) +2000, (b) +1500, (c) +1000, and (d) +500.

with CCl_4 flow. Some previous reports assigned it to LVMs related to N complexes [62, 60]. However, LVMs should not appear in this low energy region. It is more likely that it is due to some secondary phase involving nitrogen, carbon or both. It is interesting to note that no evidence of the graphite D and G modes is observed using intentional carbon dopant. This is probably related to the high growth temperature. We did not see any clear evidence of carbon point defects.

Chapter 5

Conclusions and Outlook

Epitaxial ZnO thin films grown by MOCVD on *c*-plane sapphire substrates were investigated in this work. The optical and vibrational properties of ZnO epilayers were studied using low temperature photoluminescence (PL) spectroscopy and Raman scattering spectroscopy.

Intentional incorporation of shallow group III dopants such as In and Al was demonstrated for MOCVD grown epitaxial ZnO thin films. 4.2 K PL measurements showed that the addition of controlled amounts of In and Al precursors introduced new donor bound exciton emission lines and the intensities of these additional transitions increased steadily with the flow rate of the n-type dopants.

The blue shift of the peak energies associated with these dopant impurities revealed that residual compressive strain existed in the ZnO layers due to a lattice mismatch between the ZnO crystal and the sapphire substrate. The calibration of the energy spectrum by intentional doping of In and Al allows us to identify the dominant residual donor observed by low temperature PL in our undoped ZnO material to be Ga. No evidence of hydrogen donors was observed, in contrast to previous speculation about the origin of n-type conductivity in ZnO.

4.2 K PL measurements showed that donor bound exciton transitions became much weaker and broader for ZnO epilayers grown on heat treated sapphire substrates. This indicated that pre-growth cleaning and annealing of the sapphire substrate introduces nonuniform compressive strain into the ZnO layers due to the presence of enhanced two-dimensional growth.

It was found that the incorporation of residual carbon was highly dependent on the growth temperature. Raman scattering measurements showed that sp^2 carbon nanoclusters were only present in ZnO layers grown at a temperature lower than 550 °C. Etching experiments indicated that the carbon clusters are uniformly distributed in the ZnO layers. ZnO epilayers grown at a temperature lower than 550 °C showed PL emission that was too weak to detect. In summary, epitaxial ZnO thin films grown at high temperatures showed to have a much better crystal quality with carbon impurities.

PL measurements on ZnO epilayers annealed in pure oxygen at a temperature above 800 °C (the growth temperature of the ZnO layers) showed that the group III shallow donors were quite mobile at temperatures above 800 °C. Post-growth annealing with a temperature above its growth temperature on ZnO material grown at low growth temperature could partly remove the carbon atoms by reacting with N_2O.

Intentional carbon doping was investigated on high growth-temperature epitaxial ZnO using CCl_4. Raman scattering data showed that no sp^2 carbon clusters were incorporated into the ZnO layers and a phonon mode at around 276 cm^{-1} was found to correlate with increasing CCl_4. This may indicate that this mode is related to the presence of carbon, however it is not in the correct energy range to be an LVM, and is probably due to a secondary phase. These results also revealed that the crystallinity of ZnO thin films was improved in the presence of CCl_4.

Future work should focus on the growth of ZnO thin films on ZnO substrates. As the lattice is matched between the film and the substrate in this case, there should be no strain introduced into the ZnO layers. ZnO nanowires can also be a possible direction to study. ZnO nanowires seem to be much easier to form than planar films. Intentional doping with group V dopants such as N, P, As, and Sb should be undertaken in an effort to achieve p-type doping. Additional studies to determine the microscopic structure of the Y-line which was present in many of our samples should be performed. For PL spectroscopy, more exitation power dependent PL measurements should be undertaken to help identify the unknown peaks in the spectra. Raman scattering measurements performed with a higher resolution Raman spectrometer at low temperature are also recommended to help separate the possible ZnO lattice phonon modes $A_1(TO)$ (380 cm^{-1}) and $A_1(LO)$ (574 cm^{-1}) from the sapphire Raman features.

Bibliography

[1] M.K.Gupta, N.Sinha, and B.Kumar. "p-type K-doped ZnO nanorods for optoelectronic applications". *J. Appl. Phys.*, 109:083532, 2011.

[2] D.G.Thomas. "The exciton spectrum of zinc oxide". *J. Phys. Chem. Solids*, 15:86, 1960.

[3] M.H.Huang, S.Mao, H.Feick, H.Yan, Y.Wu, H.Kind, E.Weber, R.Russo, and P.Yang. "Room-temperature ultraviolet nanowire nanolasers". *Science*, 292:1897, 2001.

[4] X.Ma, J.Pan, P.Chen, D.Li, H.Zhang, Y.Yang, and D.Yang. "Room temperature electrically pumped ultraviolet random lasing from ZnO nanorod arrays on Si". *Opt. Express*, 17:14426, 2009.

[5] Z.K.Tang, G.K.L.Wong, P.Yu, M.Kawasaki, A.Ohtomo, H.Koinuma, and Y.Segawa. "Room-temperature ultraviolet laser emission from self-assembled ZnO microcrystallite thin films". *Appl. Phys. Lett.*, 72:3270, 1998.

[6] M.Zamfirescu, A.Kavokin, B. Gil, G.Malpuech, and M.Kaliteevski. "ZnO as a material mostly adapted for the realization of room-temperature polariton lasers". *Phys. Rev. B*, 65:161205, 2002.

[7] E.Ohshima, H.Ogino, I.Niikura, K.Maeda, M.Sato, M.Ito, and T.Fukuda. "Growth of the 2-in-size bulk ZnO single crystals by the hydrothermal method". *J. Cryst. Growth*, 260:166, 2004.

[8] Y.Chen, D.M.Bagnall, H.Koh, K.Park, K.Hiraga, Z.Zhu, and T.Yao. "Plasma assisted molecular beam epitaxy of ZnO on c-plane sapphire: Growth and characterization". *J. Appl. Phys.*, 84:3912, 1998.

[9] R.D.Vispute, V.Talyansky, Z.Trajanovic, S.Choopn, M.Downes, R.P.Sharma, T.Venkatesan, M.C.Woods, R.T.Lareau, K.A.Jones, and A.A.IIiadis. "High quality crystalline ZnO buffer layers on sapphire (001) by pulsed laser deposition for III-V nitrides". *Appl. Phys. Lett.*, 70:2735, 1997.

[10] B.Hahn, G.Heindel, E.Pschorr-Schoberer, and W.Gebhardt. "MOCVD layer growth of ZnO using DMZn and tertiary butanol". *Semicond. Sci. Technol*, 13:788, 1998.

[11] A.Y.Polyakov, N.B.Smirnov, A.V.Govorkov, E.A.Kozhukhova, Y.W.Heo, M.P.Ivill, K.Ip, D.P.Norton, S.J.Pearton, J.Kelly, R.Rairigh, A.F.Hebard, and T.Steiner. "Properties of Mn- and Co-doped bulk ZnO crystals". *J. Vac. Sci. Tec. B*, 23:274, 2005.

[12] H.Maki, T.Ikoma, I.Sakaguchi, N.Ohashi, H.Haneda, J.Tanaka, and N.Ichinose. "Control of surface morphology of ZnO $(000\bar{1})$ by hydrochloric acid etching". *Thin Solid Films*, 411:91, 2002.

[13] X.Gu, M.A.Reshchikov, A.Teke, D.Johnstone, H.Morkoc, B.Nemeth, and J.Nause. "GaN epitaxy on thermally treated c-plane bulk ZnO substrates with O and Zn faces". *Appl. Phys. Lett.*, 84:2268, 2004.

[14] Robert R. Reeber and Kai Wang. "Lattice parameters and thermal expansion of important semiconductors and their substrates". *Materials Research Society Symposium*, 622:T6.35.1, 2000.

[15] T.Minami, H.Sato, H.Nanto, and S.Takata. "Group III impurity doped zinc oxide thin films prepared by RF magnetron sputtering". *Jpn. J. Appl. Phys.*, 24:L781, 1985.

[16] D.C.Look and B.Claflin. "p-type doping and devices based on ZnO". *Phys. Status Solidi B*, 241:624, 2004.

[17] W.Walukiewicz. "Defect formation and diffusion in heavily doped semiconductors". *Phys. Rev. B*, 50:5221, 1994.

[18] C.G.Van de Walle, D.B. Laks, G.F.Neumark, and S.T.Pantelides. "First-principles calculations of solubilities and doping limits: Li, Na, and N in ZnSe". *Phys. Rev. B*, 47:9425, 1993.

[19] D.C.Look, J.W.Hemsky, and J.R.Sizelove. "Residual native shallow donor in ZnO". *Phys. Rev. Lett.*, 82:2552, 1999.

[20] A.F.Kohan, G.Ceder, D.Morgan, and C.G.Van de Walle. "First-principles study of native point defects in ZnO". *Phys. Rev. B*, 61:15019, 2000.

[21] S.F.J.Cox, E.A.Davis, S.P.Cottrell, P.J.C.King, J.S.Lord, J.M.Gil, H.V.Alberto, R.C.Vilao, J.P.Duarte, N.A.Campos, A.Weidinger, R.L.Lichti, and S.J.C.Irvine. "Experimental confirmation of the predicted shallow donor hydrogen state in zinc oxide". *Phys. Rev. Lett.*, 86:2601, 2001.

[22] Jacques I.Pankove. *Optical processes in semiconductors*. Prentice-Hall Inc., 1971.

[23] B. K. Meyer, H. Alves, D. M. Hofmann, W. Kriegseis, D. Forster, F. Bertram, J. Christen, A. Hoffmann, M. Straßburg, M. Dworzak, U. Haboeck, and A. V. Rodina. "Bound exciton and donor–acceptor pair recombinations in ZnO". *Phys. Stat. Sol. (b)*, 241(2):231, 2004.

[24] B. K. Meyer, J. Sann, S. Lautenschläger, M. R. Wagner, and A. Hoffmann. "Ionized and neutral donor-bound excitons in ZnO". *Phys. Rev. B*, 76(18):184120, Nov 2007.

[25] S.J.Jiao, Y.M.Lu, D.Z.Shen, Z.Z.Zhang, B.H.Li, Z.H.Zheng anb B.Yao, J.Y.Zhang, D.X.Zhao, and X.W.Fan. "Donor–acceptor pair luminescence of nitrogen doping p-type ZnO by plasma-assisted molecular beam epitaxy". *J.Luminescence*, 122:368, 2007.

[26] L.S.Hsu, C.S.Yeh, C.C.Kuo, B.R.Huang, and S.Dhar. "Optical and transport properties of undoped and Al-, Ga- and In-doped ZnO thin films". *J. Optoelectron. Adv. M.*, 7:3039, 2005.

[27] S.Sakong and P.Kratzer. "Density functional study of carbon doping in ZnO". *Semicond. Sci. Technol.*, 26:014038, 2011.

[28] J.R.Haynes. "Experimental proof of the existence of a new electronic complex in silicon". *Phys. Rev. Lett.*, 4:361, 1960.

[29] U.Ozgur, Y.I.Alivov, A.Teke, M.A.Reshchikov, S.Dogan, V.Avrutin, S.J.Cho, and H.Morkoc. "A comprehensive review of ZnO materials and devices". *J. Appl. Phys.*, 98:041301, 2005.

[30] M.R.Wagner, G.Callsen, J.S.Reparaz, J.H.Schulze, R.Kirste, M.Cobet, I.A.Ostapenko, S.Rodt, C.Nenstiel, M.Kaiser, A.Hoffmann, A.V.Rodina, M.R.Phillips, S.Lautenschlager, S.Eisermann, and B.K.Meyer. "Bound excitons in ZnO: Structural defect complexes versus shallow impurity centers". *Phys. Rev. B*, 84:035313, 2011.

[31] D.C.Li. *Electrical properties of ZnO grown by metalorganic vapour phase epitaxy*. Master's thesis, Simon Fraser University, 2011.

[32] H.Kato, M.Sano, K.Miyamoto, and T.Yao. "Growth and characterization of Ga-doped ZnO layers on a-plane sapphire substrates grown by molecular beam epitaxy". *J. Cryst. Growth*, 237:538, 2002.

[33] S.Y.Myong, S.J.Baik, C.H.Lee, W.Y.Cho, and K.S.Lim. "Extremely transparent and conductive ZnO:Al thin films prepared by photo-assisted metalorganic chemical vapor deposition (photo-MOCVD) using $AlCl_3(6H_2O)$ as new doping material". *Jpn. J. Appl. Phys.*, 36:L1078, 1997.

[34] T. Ben-Yaacov, T. Ive, C. Van de Walle, U. Mishra, J. Speck, and S. Denbaars. "Properties of In-doped ZnO films grown by metalorganic chemical vapor deposition on GaN(0001) templates". *J. Electronic Materials*, 39:608, 2010. 10.1007/s11664-009-1022-x.

[35] A.Valentini, F.Quaranta, M.Rossi, and G.Battaglin. "Preparation and characterization of Li-doped ZnO films". *J. Vac. Sci. Technol. A*, 9:286, 1991.

[36] S.Heitsch, C.Bundesmann, G.Wagner, G.Zimmermann, A.Rahm, H.Hochmuth, G.Benndorf, H.Schmidt, M.Schubert, M.Lorenz, and M.Grundmann. "Low temperature photoluminescence and infrared dielectric functions of pulsed laser deposited ZnO thin films on silicon". *Thin Solid Films*, 496:234, 2006.

[37] S.H.Jeong, B.S.Kim, and B.T.Lee. "Photoluminescence dependence of ZnO films grown on Si(100) by radio-frequency magnetron sputtering on the growth ambient". *Appl. Phys. Lett.*, 82:2625, 2003.

[38] X.W.Sun and H.S.Kwok. "Optical properties of epitaxially grown zinc oxide films on sapphire by pulsed laser deposition". *J. Appl. Phys.*, 86:408, 1999.

[39] M.R.Wagner, H.W.Kunert, A.G.J.Machatine, A.Hoffmann, P.Niyongabo, J.Malherbe, and J.Barnas. "Bound and free excitons in ZnO. Optical selection rules in the absence and presence of time reversal symmetry". *Microelectronics Journal*, 40(2):289, 2009.

[40] M.Biswas, Y.S.Jung, H.K.Kim, K.Kumar, G.J.Hughes, S.Newcomb, M.O.Henry, and E.McGlynn. "Microscopic origins of the surface exciton photoluminescence peak in ZnO nanostructures". *Phys. Rev. B*, 83:235320, 2011.

[41] J.Grabowska, A.Meaney, K.K.Nanda, J.P.Mosnier, M.O.Henry, J.R.Duclere, and E.McGlynn. "Surface excitonic emission and quenching effects in ZnO nanowire/nanowall systems: Limiting effects on device potential". *Phys. Rev. B*, 71:115439, 2005.

[42] L.Wischmeier, T.Voss, I.Ruckmann, and J.Gutowski. "Dynamics of surface-excitonic emission in ZnO nanowires". *Phys. Rev. B*, 74:195333, 2006.

[43] C.G.Van de Walle. "Hydrogen as a cause of doping in zinc oxide". *Phys. Rev. Lett.*, 85:1012, 2000.

[44] A.Janotti and C.G.Van de Walle. "Hydrogen multicentre bonds". *Nature Mater.*, 6:44, 2007.

[45] E. V. Lavrov, F. Herklotz, and J. Weber. "Identification of two hydrogen donors in ZnO". *Phys. Rev. B*, 79(16):165210, Apr 2009.

[46] C.G.Van de Walle. "Defect analysis and engineering in ZnO". *Physica B*, 308:899, 2001.

[47] Markus R. Wagner, Til P. Bartel, Ronny Kirste, Axel Hoffmann, Joachim Sann, Stefan Lautenschläger, Bruno K. Meyer, and C. Kisielowski. "Influence of substrate surface

polarity on homoepitaxial growth of ZnO layers by chemical vapor deposition". *Phys. Rev. B*, 79(3):035307, Jan 2009.

[48] J.Wrzesinski and D.Frohlich. "Two-photon and three-photon spectroscopy of ZnO under uniaxial stress". *Phys. Rev. B*, 56:13087, 1997.

[49] T.B.Bateman. "Elastic moduli of single-crystal zinc oxide". *J. Appl. Phys.*, 33:3309, 1962.

[50] Y.Zhang, B.Lin, X.Sun, and Z.Fu. "Temperature-dependent photoluminescence of nanocrystalline ZnO thin films grown on Si (100) substrates by the sol-gel process". *Appl. Phys. Lett.*, 86:131910, 2005.

[51] L.Wang and N.C.Giles. "Temperature dependence of the free-exciton transition energy in zinc oxide by photoluminescence excitation spectroscopy". *J. Appl. Phys.*, 94:973, 2003.

[52] B.Cao, W.Cai, and H.Zeng. "Temperature-dependent shifts of three emission bands for ZnO nanoneedle arrays". *Appl. Phys. Lett.*, 88:161101, 2006.

[53] Y.J.Zhang, C.S.Xu, Y.C.Liu, Y.X.Liu, G.R.Wang, and X.W.Fan. "Temperature-enchanced ultraviolet emission in ZnO thin film". *J. Luminescence*, 119:242, 2006.

[54] T.Minami, T.Miyata, Y.Ohtani, and Y.Mochizuki. "New transparent conducting Al-doped ZnO film preparation techniques for improving resistivity distribution in magnetron sputtering deposition". *Jpn. J. Appl. Phys.*, 45:L409, 2006.

[55] M. A. Stroscio and M. Dutta. *Phonons in nanostructures*. Cambridge University Press, 2001.

[56] P.Y.Yu and D.h.c.M.Cardona. *Fundamentals of Semiconductors: Physics and Materials Properties*. Springer, 2001.

[57] M.D.McCluskey. "Local vibrational modes of impurities in semiconductors". *J. Appl. Phys.*, 87:3593, 1999.

[58] L.L.Kerr, X.Li, M.Canepa, and A.J.Sommer. "Raman analysis of nitrogen doped ZnO". *Thin Solid Films*, 515:5282, 2007.

[59] H.Chen, S.Gu, W.Liu, S.Zhu, and Y.Zheng. "Influence of unintentional doped carbon on growth and properties of N-doped ZnO films". *J. Appl. Phys.*, 104:113511, 2008.

[60] A.Kaschner, U.Haboeck, M.Strassburg, M.Strassburg, G.Kaczmarczyk, A.Hoffmann, C.Thomsen, A.Zeuner, H.R.Alves, D.M.Hofmann, and B.K.Meyer. "Nitrogen-related local vibrational modes in ZnO:N". *Appl. Phys. Lett.*, 80:1909, 2002.

[61] N.H.Nickel, F.Friedrich, J.F.Rommeluere, and P.Galtier. "Vibrational spectroscopy of undoped and nitrogen-doped ZnO grown by metalorganic chemical vapor deposition". *Appl. Phys. Lett.*, 87:211905, 2005.

[62] K.Tang, S.Gu, S.Zhu, W.Liu, J.Ye, J.Zhu, R.Zhong, Y.Zheng, and X.Sun. "Carbon clusters in N-doped ZnO by metal-organic chemical vapor deposition". *Appl. Phys. Lett.*, 93:132107, 2008.

[63] A.C.Ferrari and J.Robertson. "Interpretation of Raman spectra of disordered and amorphous carbon". *Phys. Rev. B*, 61:14095, 2000.